Uncovering Subtle GNSS Spoofing by Decomposing the Complex Cross Ambiguity Function

SAHIL AHMED
Illinois Institute of Technology, Chicago, IL, USA

SAMER KHANAFSEH, Member, IEEE
Illinois Institute of Technology, Chicago, IL, USA

BORIS PERVAN, Senior Member, IEEE
Illinois Institute of Technology, Chicago, IL, USA

***Abstract*— In this paper, we introduce a method to uncover Global Navigation Satellite System (GNSS) spoofing by directly decomposing the Complex Cross Ambiguity Function (CCAF) into its authentic and counterfeit components. We demonstrate the importance of using complex cross ambiguity measurements compared to the magnitude-only approaches utilized in prior work on spoofing detection. We also introduce a CCAF error decorrelation method to mitigate the influence of thermal noise. The detector can identify spoofing in the presence of multipath and when the spoofing signal is power-matched with offsets in code delay and Doppler frequency that are close to the authentic signal.**

***Index Terms*— GNSS spoofing detection, cross ambiguity function, particle swarm decomposition, aviation safety, navigation integrity, PNT resilience.**

Manuscript received July 18, 2024; revised XXXXX 00, 0000; accepted XXXXX 00, 0000.
"This work was supported in part by the Federal Aviation Administration (FAA) under MOA 693KA8-21-T-00027 and the Center for Assured and Resilient Navigation in Advanced TransportatION Systems (CARNATIONS) under the US Department of Transportation (USDOT)'s University Transportation Center (UTC) program under Grant 69A3552348324." *(Corresponding author: Sahil Ahmed).*

Sahil Ahmed, Samer Khanfseh and Boris Pervan are with the Illinois Institute of Technology Chicago, IL 60616 USA. E-mail: (sahmed53@hawk.iit.edu, khansam1@iit.edu, pervan@iit.edu).

0018-9251 © 2024 IEEE

I. INTRODUCTION

Global Navigation Satellite Systems (GNSS) are utilized for positioning, navigation, and timing (PNT) services worldwide, with applications spanning aviation, automated vehicle systems, telecommunications, finance, and energy systems. However, GNSS signals are susceptible to radio frequency interference (RFI), including jamming and spoofing attacks. Jamming can disrupt access to GNSS services, while spoofing can create inaccurate positioning and timing estimates, which in transportation applications can lead to dangerous results. The nomenclature for RFI threats, both jamming and spoofing, has been categorized into various levels according their severity and sophistication in [1]. This paper focuses on detecting *targeted* spoofing attacks wherein a malicious actor manipulates the victim's position and/or time solution by broadcasting counterfeit GNSS signals [1], [2]. We address the most challenging scenario where the attacker tracks the target to initially align the spoofed signal closely with the authentic one to avoid easy detection.

Different methods have been proposed to detect spoofing, such as: received power monitoring, which monitors the response of automatic gain control (AGC) [3] to detect when an overpowered spoofing signal is broadcast; signal quality monitoring (SQM) [4], which tracks the distortion of the autocorrelation function; Receiver Autonomous Integrity Monitoring (RAIM) checks on inconsistent sets of five or more pseudoranges to allow the receiver to detect spoofing with one or (sometimes) more false signals [5]; signal direction of arrival (DoA) estimation techniques using directional antennas, or moving antennas, in a specified pattern to observe if all satellite signals are broadcast from the same direction [6]; inertial navigation system (INS) aiding [7], which is based on position deviation monitoring; authenticated signal architectures, which propose to verify the incoming signals with a public key [8]; machine learning approaches [9]; and others [10]. Each of these methods has its own advantages and drawbacks.

Received power monitoring and Signal Quality Monitoring (SQM) can easily detect simple spoofing scenarios. However, sophisticated spoofers can adjust the power of their signals to closely match legitimate signals and create signals with minimal distortion, making detection difficult for these methods. Receiver Autonomous Integrity Monitoring (RAIM) can be used only if one or two satellite signals are compromised, but if all signals are spoofed, RAIM will not be able to detect spoofing. Signal Direction of Arrival (DoA) estimation requires specialized directional or moving antennas, which increases system complexity and cost. These antennas are also limited by form factor restrictions of the GNSS application. INS systems are prone to drift over time, which can affect the accuracy of spoofing detection and are also subject to the quality of INS and the duration of the spoofing scenario. Adding INS to GNSS receivers also increases both the cost and complexity of the system. Authenticated signal

architectures require significant changes to existing GNSS infrastructure to support signal authentication, meaning new signal structures have to be designed with backward compatibility to support existing receivers. Machine learning approaches require large amounts of training data to be effective, which can be challenging to obtain. Additionally, machine learning models will struggle to adapt to new spoofing techniques not present in the training data.

Methods for spoofing detection based on Cross Ambiguity Function (CAF) monitoring have also been recently investigated [9] [11]. Notably, they exploit only the magnitude of the full *Complex* CAF (CCAF). A sampled signal can be represented in the form of a complex number, I (in-phase) and Q (quadrature), as a function of code delay and Doppler offset. In existing CAF monitoring concepts, a receiver performs a two-dimensional sweep to calculate the CAF by correlating the received signal with a locally generated carrier modulated by pseudorandom code for different possible code delay and Doppler pairs. Spoofing is detectable when two peaks are distinguishable in the CAF measurement space. This could happen, for example, if a power-matched spoofed signal does not accurately align the Doppler and code delay with the authentic received signal. In practice, detection using the CAF is not reliable under multipath or if the spoofed signals are close to the authentic ones. In our work, we instead exploit the full CCAF.

We can decompose a CCAF made up of N contributing signals by minimizing a least-squares cost function [12], [13]. Because the optimization problem is non-convex, we implement a Particle Swarm Optimization (PSO) algorithm to find the global minimum. The algorithm can decompose the received combination of GNSS signals for a given satellite (e.g., authentic, spoofed, and multipath) into its respective defining parameters: signal amplitudes, Doppler frequencies, code delays, and carrier phases. To minimize the impact of thermal noise in the CCAF decomposition, we set the pre-detection integration time to the upper boundary limit imposed by the bit length of modulated data on the GNSS signal, and we explicitly account for the correlation of thermal noise across the code delay and Doppler measurement space [14]. A similar concept is used in the multipath estimating delay lock loop (MEDLL) described in [15]; however, it uses only the real part of the signal, does not account measurement correlation and cannot deal with spoofing.

Achieving precise carrier phase matching between signals will be extremely difficult for the spoofer in real-world scenarios. We exploit this weakness with the CCAF through the direct use of both the in-phase (real) and quadrature (imaginary) components of the signal. After decomposition of the signal for a given satellite we have three extracted code delays and carrier phases corresponding to the authentic, spoofed, and multipath components.

It is worth noting that while the decomposed CCAF provides the means to detect spoofing, it does not by itself provide a way to identify which signal is authentic and which is spoofed. However, this can partially be addressed by generating least-squares position estimates using all combinations of the decomposed code delays and carrier phases for all the satellites currently being tracked. Out of all the combination sets, only two will be consistent in a RAIM sense: when all the authentic signals from each satellite are grouped together in one set, and all the spoofed signals from each satellite are together in another. The multipath code delays and carrier phases would not be self-consistent across the satellite channels. The process is termed "Inverse RAIM" because the authentic/spoofed signal grouping is based on observing an extra set "passing" the RAIM test [13]. Integrating an inertial measurement unit (IMU) and/or receiver clock dynamic models can further enable identification and rejection of the spoofed signals and continuous tracking of the authentic ones [16].

In this paper, we focus specifically on the method to decompose the CCAF into its component signals (authentic, spoofed, and multipath). In doing so, we show that the effects of code cross-correlation are small relative to those due to thermal noise. Then, to account for and mitigate the effects of the latter, we introduce a new CCAF error decorrelation method. Spoofing detection/resistance performance is then validated against carefully constructed spoofing scenarios. Post-decomposition monitor actions are outside the scope of this paper, but interested readers can refer to [16] for details on some of the ideas briefly noted in the previous paragraph.

The remainder of this paper is organized as follows: Section II provides background on the CCAF and its computation, Section III describes CCAF measurement errors, Section IV develops the targeted spoofing scenario, Section V explains the CCAF decomposition methodology, Section VI details the CCAF error decorrelation method, Section VII provides a covariance analysis predicting improved performance using decorrelated CCAF measurements compared to correlated CCAF measurements, Section VIII presents actual CCAF decomposition results for both correlated and decorrelated measurements, and Section IX summarizes the work.

II. COMPLEX CROSS AMBIGUITY FUNCTION

The CCAF measurement space discretely spans code delay ($\bar{\tau}$) and Doppler frequency ($\bar{f}_D$). The CCAF itself can be expressed in as an $m \times n$ complex matrix

$$CCAF = \begin{bmatrix} I_{11}+jQ_{11} & I_{12}+jQ_{12} & \cdots & I_{1n}+jQ_{1n} \\ I_{21}+jQ_{21} & I_{22}+jQ_{22} & \cdots & I_{2n}+jQ_{2n} \\ \vdots & \vdots & \vdots & \vdots \\ I_{m1}+jQ_{m1} & I_{m2}+jQ_{m2} & \cdots & I_{mn}+jQ_{mn} \end{bmatrix}, \quad (1)$$

where the in-phase and quadrature components represent the real and imaginary parts of the signal, respectively,

and the Doppler frequency ($\bar{f}_D$) varies from rows 1 to m and the code delay ($\bar{\tau}$) from columns 1 to n. The . The upper limit on the code delay dimension is the length of the code itself, and the Doppler frequency is well within ±5000 Hz. The in-phase I and quadrature Q components of an uncorrupted signal (i.e., no spoofing, multipath, or thermal noise) with code delay (τ), Doppler (f_D), carrier phase θ, and amplitude $\sqrt{C}$ are shown in Equations (2) and (3) and combined in the complex representation in (4).

$$I\left(\sqrt{C},\tau,f_D,\theta;\bar{\tau},\bar{f}_D,\bar{\theta}\right) = \frac{\sqrt{C}}{T}\int_0^T c(t-\tau)c(t-\bar{\tau}) \cdot \cos\left(2\pi\left(f_D-\bar{f}_D\right)t+\theta-\bar{\theta}\right)dt \tag{2}$$

$$Q\left(\sqrt{C},\tau,f_D,\theta;\bar{\tau},\bar{f}_D,\bar{\theta}\right) = \frac{\sqrt{C}}{T}\int_0^T c(t-\tau)c(t-\bar{\tau}) \cdot \sin\left(2\pi\left(f_D-\bar{f}_D\right)t+\theta-\bar{\theta}\right)dt \tag{3}$$

$$S = I + iQ \tag{4}$$

To limit the size of the measurement data, we constrain the carrier phase measurement space to $\bar{\theta}=0$. However, as we will demonstrate later, this does not prevent accurate estimation of the true phase θ. For Global Positioning System (GPS) signals, the integration time T can range from 1 to 20 milliseconds, with the upper limit set to avoid integration across boundaries of a GPS data bit. Integration is performed to reduce the effects of thermal noise. Without data modulation (e.g., a pilot signal) longer coherent integration times may also be limited by satellite and receiver oscillator (clock) phase noise and receiver motion. Performing the integrals in Equations (2) and (3), Equation (4) can be expressed as (5)

$$S\left(\sqrt{C},\tau,f_D,\theta;\bar{\tau},\bar{f}_D,\bar{\theta}\right) = \sqrt{C}R(\tau-\bar{\tau})\,\mathrm{sinc}\left(\pi\left(f_D\ -\bar{f}_D\right)T\right) \cdot \exp\left(i\pi\left(\left(f_D-\bar{f}_D\right)T\ +\theta-\bar{\theta}\right)\right), \tag{5}$$

where

$$R(\xi) = \begin{cases} \frac{\xi}{T_c}+1 & -T_c<\xi<0 \\ \frac{-\xi}{T_c}+1 & 0<\xi<T_c \\ 0 & \text{otherwise} \end{cases} \tag{6}$$

and T_c is the duration of a single code chip. Strictly speaking, Equation (6) is true only for infinite length random codes. For finite length pseudorandom noise (PRN) codes like GPS L1 C/A, $R(\xi)$ will vary slightly (and differently for each satellite) from Equation (6). Figure 1 shows the actual functions; these will be used in the decompositions described later.

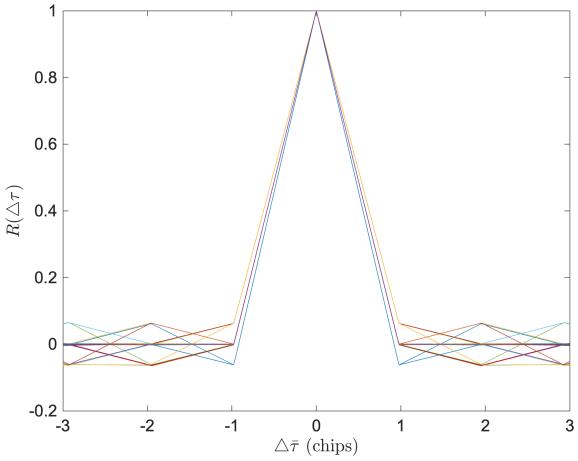

Fig. 1. The GPS L1 C/A CCAF as a function code delay.

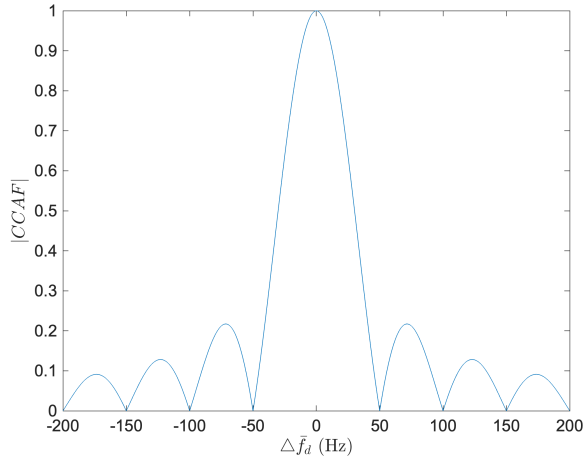

Fig. 2. Magnitude of the GPS L1 C/A CCAF for $T=20$ ms as a function of Doppler offset.

To simplify the notation, we define the amplitude $a \triangleq \sqrt{C}$. Summing N component signals (for example, assuming an authentic satellite signal, a spoofed signal, and a single multipath signal, $N=3$), we have

$$S_N(x\,|\,\bar{\tau},\bar{f}_D,\bar{\theta}) = \sum_{l=1}^{N} a_l R\left(\tau_l-\bar{\tau}\right)\mathrm{sinc}\left(\pi\left(f_{D_l}-\bar{f}_D\right)T\right) \cdot \exp\left(i\pi\left(f_{D_l}-\bar{f}_D\right)T+\left(\theta_l-\bar{\theta}\right)\right), \tag{7}$$

where $x \triangleq (a_1,\tau_1,f_{D_1},\theta_1,\ \ldots,\ a_N,\tau_N,f_{D_N},\theta_N)$.

When viewed from the perspective of code delay, the CCAF is represented by the autocorrelation functions in Figure 1. From the viewpoint of Doppler frequency, the magnitude of the CCAF is represented by a sinc function, as illustrated in Figure 2 for $T=20$ ms.

In the absence of spoofing, multipath, thermal noise, and code cross-correlation effects, the GPS C/A CCAF measurement space looks like Figure 3, in this case for measurement spacings of $\bar{f}_D=12.5$ Hz and $\bar{\tau}=0.02$

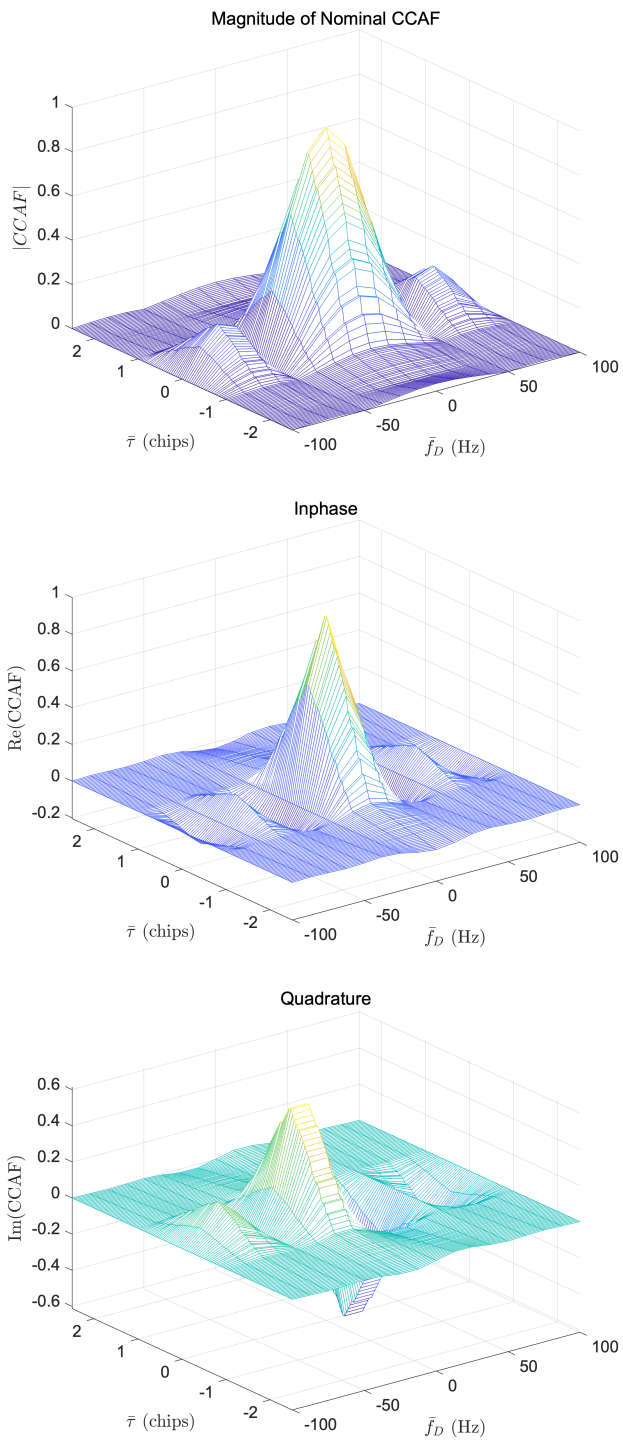

Fig. 3. Magnitude (top), in-phase (middle) and quadrature (bottom) components of the nominal GPS L1 C/A CCAF without thermal noise or code cross-correlation.

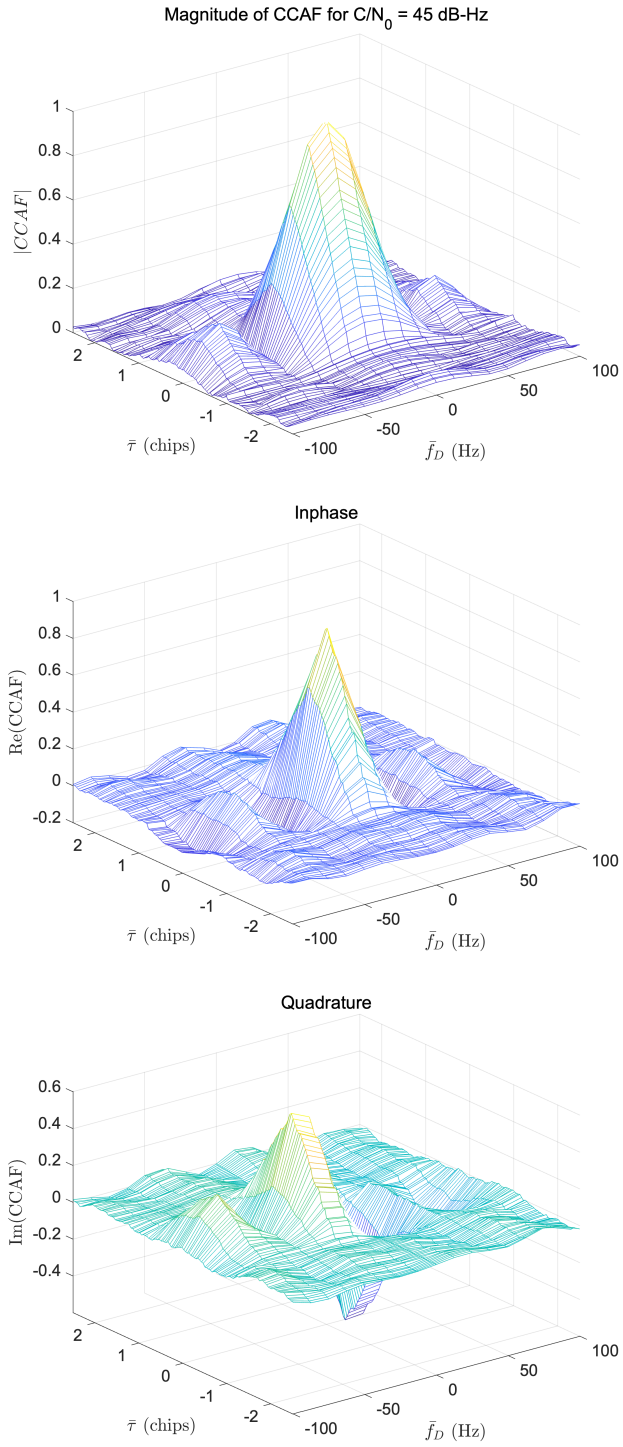

Fig. 4. Magnitude (top), in-phase (middle) and quadrature (bottom) component of the nominal GPS L1 C/A CCAF with code cross-correlation and thermal noise with C/N_0 = 45 dB-Hz.

chips. Utilizing a software-defined radio [16] provides flexibility to arbitrarily adjust Doppler spacing. However, the spacing of code delays is limited by the sampling rate of the receiver's front end. Figure 4 shows the same no-spoofing, no-multipath case but with code cross-correlation of 12 satellites and thermal noise (C/N_0= 45 dB-Hz) included. The real and imaginary parts of the CCAF measurement space are clearly affected. These errors will be discussed in detail in the next section.

III. MEASUREMENT ERROR EFFECTS

Multipath occurs when a satellite signal is reflected off a surface and reaches the receiving antenna. We account

for the presence of multipath directly as an additional component signal in the decomposition of the CCAF. However, the contributions of code cross-correlation and thermal noise to the CCAF cannot be treated so directly.

The L1 frequency band is used by multiple GPS satellites transmitting simultaneously. The L1 carrier signals are modulated with the C/A codes using Binary Phase Shift Keying (BPSK) at a chip rate of 1.023 MHz, with the code repeating every 1 ms. The C/A codes are designed to be nearly orthogonal, meaning they have strong autocorrelation and minimal cross-correlation properties, though they are not completely orthogonal. GPS receivers track multiple satellites simultaneously, typically between 6 and 11, depending on the time of day and user location. To observe the effect of C/A code cross-correlation, Figure 5 shows the magnitude of the CCAF with code cross-correlation for 6 satellites and for 12 satellites. Comparing with the uppermost plot of Figure 3, the effects of cross-correlation are not significant, at least not in the $\{\bar{f}_D, \bar{\tau}\}$ space of interest. (Recall we are interested in addressing difficult-to-detect scenarios where the code delay and Doppler frequency of the spoofed signal are close to the authentic signal's.)

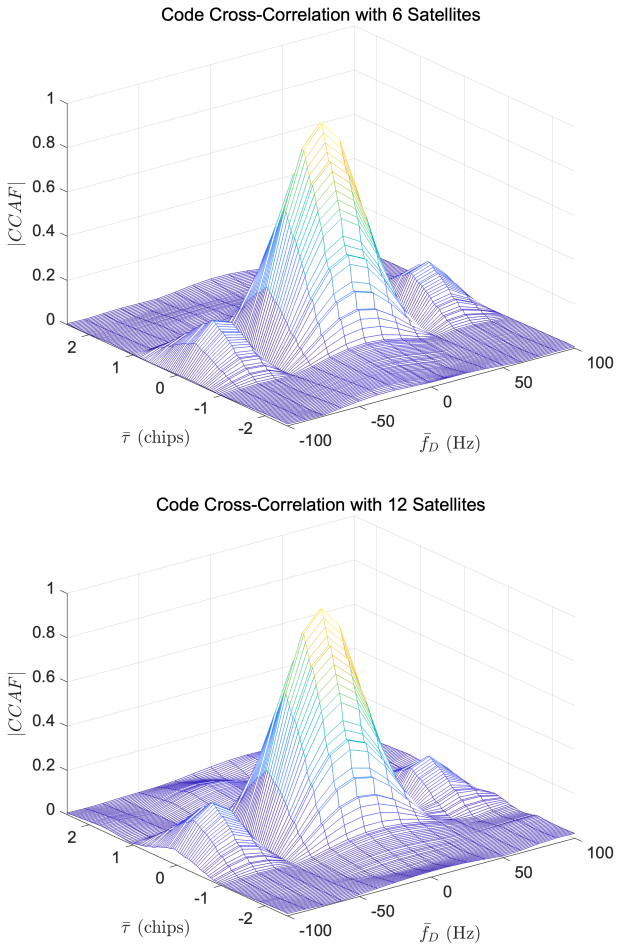

Fig. 5. Magnitudes of the GPS L1 C/A CCAF for $T = 20$ ms in presence of code cross correlation with 6 (top) and 12 (bottom) satellites.

Thermal noise, inherent in all electronic devices, affects the receiver's ability to accurately detect and process the L1 signal. Figure 6 displays the CCAF magnitude, without code cross-correlation, for C/N_0 values of 45 dB-Hz and 35 dB-Hz. In Figure 7, we combine both code cross-correlation with 12 satellites and thermal noise, plotting the CCAF magnitude for C/N_0 values of 45 dB-Hz and 35 dB-Hz. Again, it is evident that code cross-correlation does not contribute significantly. However, decreasing C/N_0 from 45 dB-Hz to 35 dB-Hz causes a considerable increase in the noise floor. To minimize the effects of thermal noise, measurement error decorrelation (whitening) should be performed before attempting signal decomposition. Section VI will later describe how to do this.

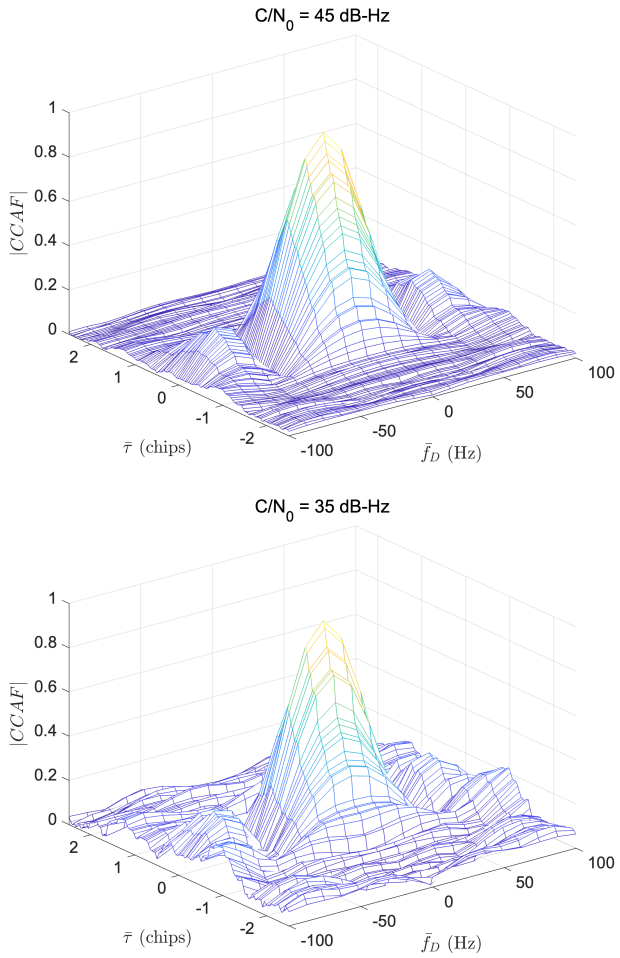

Fig. 6. Magnitudes of the GPS L1 C/A CCAF for $C/N_0 = 45$ dB-Hz (top) and $C/N_0 = 35$ dB-Hz (bottom) and $T = 20$ ms without code cross-correlation.

IV. SPOOFING

GNSS spoofing techniques consist of broadcasting counterfeit signals with the goal of taking control of a GNSS receiver and producing false results for positioning or timing or both. To avoid easy detection, a sophisticated spoofing attack would replicate and transmit signals with

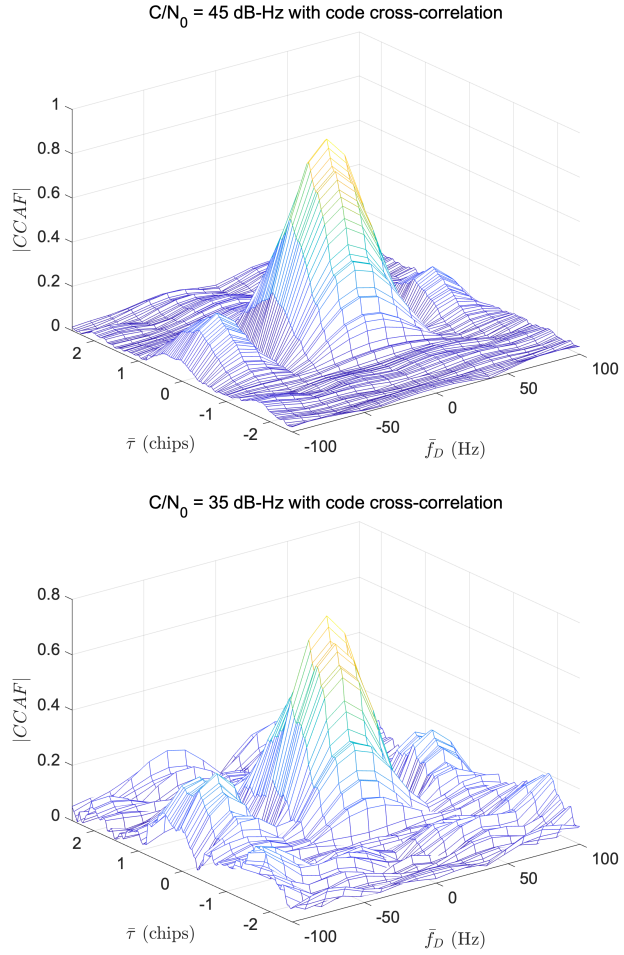

Fig. 7. Magnitudes of the GPS L1 C/A CCAF for $C/N_0 = 45$ dB-Hz (top) and $C/N_0 = 35$ dB-Hz (bottom) and $T = 20$ ms with code cross-correlation.

code delays and Dopplers initially very close to the authentic signals. However, it is very hard to replicate the carrier phase precisely, and we exploit weakness by observing both the real and imaginary signal contributions in CCAF. In the subtle spoofing attack just noted, the spoofer first generates a signal with nearly the same code delay and Doppler frequency as the authentic signal, and then slowly pulls away in code delay, Doppler, or both.

When a spoofed signal is present and the code delays and Doppler frequencies of the signals are not closely aligned, two peaks are visible in the magnitude of the CCAF. A scenario like this is shown in Figure 8 along with the real and imaginary parts of CCAF. In this case, existing CAF monitoring approaches can potentially be effective [10] [11]. However, the two peaks merge if the code delays and Doppler frequencies are closely aligned, as illustrated in Figure 9. Here the spoofed and authentic signals have equal amplitude but differ in code delay (τ) by 0.2 chips (60 m offset for the GPS C/A Code), Doppler (f_D) by 10 Hz (2 m/s offset for the GPS L1 carrier), and carrier phase (θ) by 90 degrees.

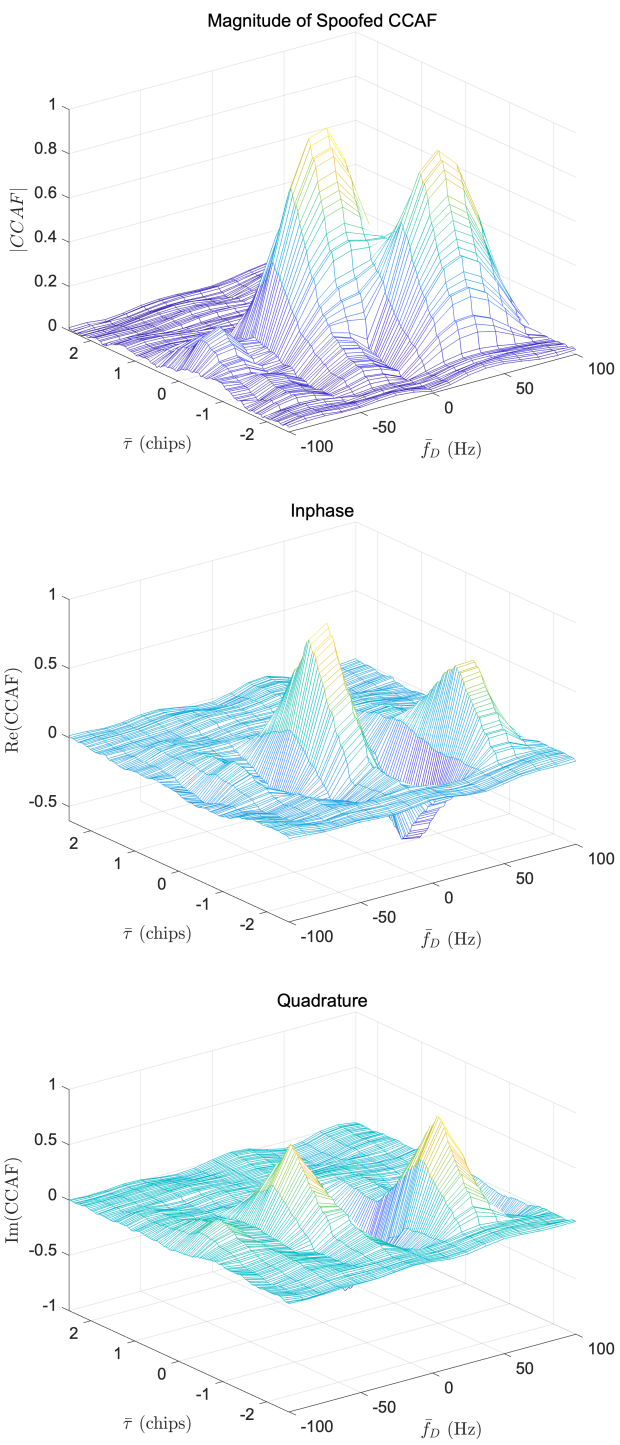

Fig. 8. Magnitude (top), in-phase (middle) and quadrature (bottom) components of the spoofed GPS L1 C/A CCAF for $C/N_0 = 45$ dB-Hz and $T = 20$ ms with code cross-correlation when code delays and Doppler frequencies of the authentic and spoofed signals are far apart.

V. CCAF DECOMPOISTION

To decompose the CCAF into its constituents, we incorporate an optimization algorithm which searches for the best match of the CCAF measurement space to the basis functions in Equation (7) – with the correct $R(\Delta\tau)$

functions for the individual satellites (cf. Figure 1) – by adjusting the amplitude, Doppler frequency, code delay, and carrier phase parameters for each signal. Stacking the CCAF measurements from the grid space $\bar{\tau}, \bar{f}_D$, the measurement model can be written as

$$z = S_N(x|\bar{\tau}, \bar{f}_D) + \nu, \tag{8}$$

where ν is the vector of measurement errors, including thermal noise and the (smaller) effects of code cross-correlation. To decompose the N signals, we seek to obtain an estimate of the parameter vector, $\hat{x}$, that minimizes the cost function

$$J = ||z - S_N(\hat{x}|\bar{\tau}, \bar{f}_D)||^2. \tag{9}$$

Unfortunately, due to the structure of S_N, J is non-convex, and a global minimum cannot be obtained by standard gradient-based methods. Still, there are variety of useful techniques designed to deal with such problems. Here we use Particle Swarm Optimization (PSO) [18], which is a modern optimization algorithm that works by randomly generating (with upper and lower bounds) a population ("swarm") of candidate solutions ("particles") whose iterative movements are informed by local (particle) and global (swarm) evaluations of the cost function. The search mechanism of the PSO algorithm is explained in Appendix A.

The PSO algorithm is applied to minimize the cost function J in Equation (9). As the measurement vector z may be comprised of N signals, the parameter vector $\hat{x} = (\hat{a}_1, \hat{\tau}_1, \hat{f}_{D_1}, \hat{\theta}_1, \ \ldots, \ \hat{a}_N, \hat{\tau}_N, \hat{f}_{D_N}, \hat{\theta}_N)$ that yields the best global solution defines our CCAF decomposition.

To demonstrate this, we create an example CCAF consisting of three signals: authentic, spoofed and multipath, denoted by the subscripts 1, 2 and 3, respectively. The amplitudes of the first two signals are deliberately closely matched with values of 1 (authentic) and 0.9 (spoofed). The multipath amplitude was set lower at 0.3. The authentic and spoofed signals differ in code delay by 0.2 chips and in Doppler by 10 Hz. They are also 180 degrees out of phase with each other. The resulting CCAF measurement space (magnitude only) is shown in Figure 10. The carrier to noise density ratio C/N_0 is set at 55 dB-Hz. Table 1 shows the true parameters (x) alongside the signal parameters $(\hat{x})$ estimated by the PSO algorithm. The output parameters closely match the true parameters.

In next example, the CCAF measurement space in Figure 11 is composed of two signals but the PSO algorithm attempts to find three signals. Table 2 shows the results. The output parameters of the authentic and spoofed signals are same as the true parameters, and the third signal's amplitude is nearly zero, which means that only the two signals actually present were effectively extracted.

It is important to clarify that while we only show plots of the magnitude of the CCAF in the previous two figures (i.e., the standard CAF) the full complex measurement space is used in the decomposition. To demonstrate the importance of using the complex (CCAF) measurements relative to magnitude only (CAF), we run the same example using only the magnitude measurements observed in Figure 11. The results are in Table 3, showing that three signals are extracted at roughly equal amplitude, even though only two signals were actually present.

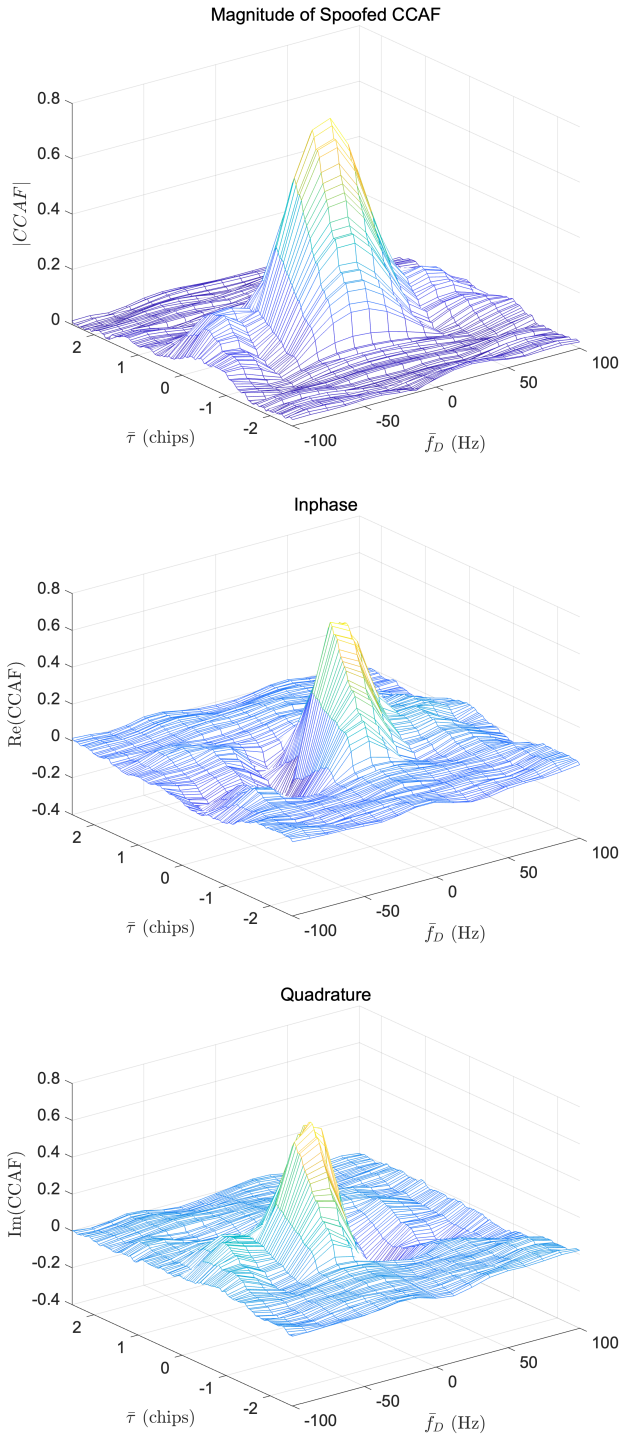

Fig. 9. Magnitude (top), in-phase (middle) and quadrature (bottom) components of the spoofed GPS L1 C/A CCAF for $C/N_0 = 45$ dB-Hz and $T = 20$ ms with code cross-correlation when code delays and Doppler frequencies of the authentic and spoofed signals are near each other.

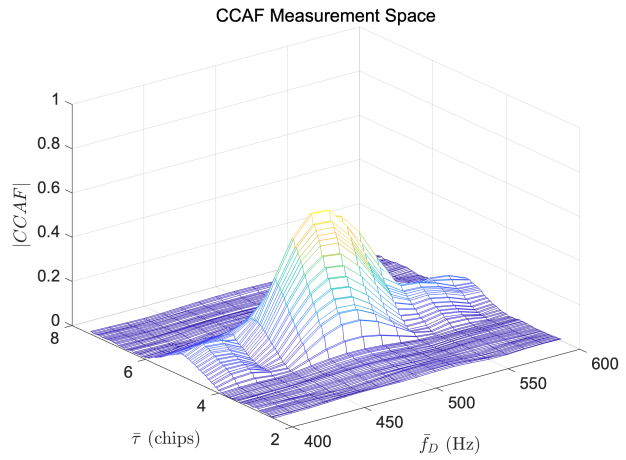

Fig. 10. Magnitude of the spoofed GPS L1 C/A CCAF for $C/N_0 = 55$ dB-Hz and $T = 20$ ms when 3 signals are present in CCAF measurement space

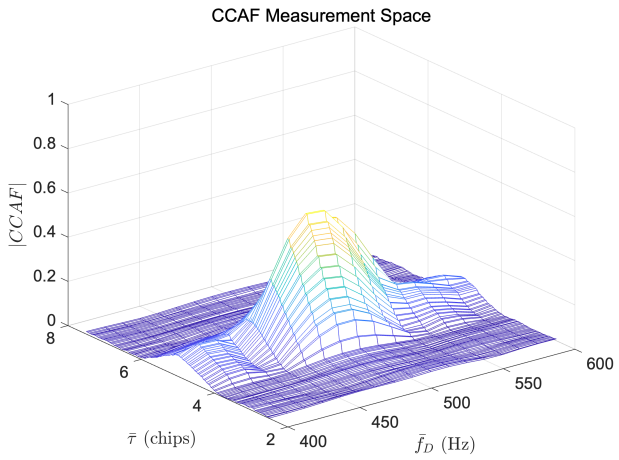

Fig. 11. Magnitude of the spoofed GPS L1 C/A CCAF for C/N_0 = 55 dB-Hz and $T = 20$ ms when 2 signals are present in CCAF measurement space.

Signal	Parameter	x (true)	$\hat{x}$ (output)
Satellite	a_1	1	0.99
	τ_1	4.9	4.89
	f_{D1}	495	494.63
	θ_1	0	6.28
Spoofed	a_2	0.9	0.89
	τ_2	5.1	5.10
	f_{D2}	505	505.35
	θ_2	3.14	3.14
Multipath	a_3	0.3	0.31
	τ_3	4.8	4.80
	f_{D3}	490	491.63
	θ_3	1.57	1.56

Table 1: A table showing the input and output parameters of the GPS L1 C/A CCAF for C/N_0 = 55 dB-Hz and $T = 20$ ms when 3 signals are present in CCAF measurement space. The units are a (unitless), τ (chips), f_D (Hz), θ (rad).

Signal	Parameter	x (true)	$\hat{x}$ (output)
Satellite	a_1	1	1.01
	τ_1	4.9	4.90
	f_{D1}	495	495.02
	θ_1	0	6.26
Spoofed	a_2	0.9	0.90
	τ_2	5.1	5.09
	f_{D2}	505	505.09
	θ_2	3.14	3.09
Multipath	a_3	0	0.01
	τ_3	0	3.52
	f_{D3}	0	509.55
	θ_3	0	6.28

Table 2: A table showing the input and output parameters of the GPS L1 C/A CCAF for C/N_0 = 55 dB-Hz and $T = 20$ ms when full CCAF is utilized in cost function with 2 signals present in CCAF measurement space. The units are a (unitless), τ (chips), f_D (Hz), θ (rad).

Signal	Parameter	x (true)	$\hat{x}$ (output)
Satellite	a_1	1	0.29
	τ_1	4.9	4.78
	f_{D1}	495	482.30
	θ_1	0	2.16
Spoofed	a_2	0.9	0.23
	τ_2	5.1	4.88
	f_{D2}	505	496.90
	θ_2	3.14	4.62
Multipath	a_3	0	0.27
	τ_3	0	5.26
	f_{D3}	0	517.31
	θ_3	0	6.23

Table 3: A table showing the input and output parameters of the GPS L1 C/A CCAF for C/N_0 = 55 dB-Hz and $T = 20$ ms when only the magnitude of CCAF is utilized in the cost function with 2 signals present in CCAF measurement space. The units are a (unitless), τ (chips), f_D (Hz), θ (rad).

Next, we decrease C/N_0 to 45 dB-Hz in Figure 12. The results are presented in Table 4, where the impact of the increased thermal noise becomes evident as the estimated parameters deviate from the true values. To help counteract the adverse effects of thermal noise, we next introduce a method to decorrelate the measurements (and modify our cost function) prior to CCAF decomposition.

VI. MEASUREMENT MODELING

We reshape the CCAF as expressed in Equation (8) as a $2mn \times 1$ measurement vector z with measurement error due to thermal noise normally distributed as $\mathbb{N}(0, V\sigma^2)$:

$$z \triangleq CCAF = \begin{bmatrix} I_{11} & Q_{11} & \dots & I_{m1} & Q_{m1} \\ I_{12} & Q_{12} & \cdots & I_{m2} & Q_{m2} & \cdots & I_{mn} & Q_{mn} \end{bmatrix}^T \tag{10}$$

The measurement error covariance matrix is $V\sigma^2$, with V defined in Equation (11) and its components in Equations (12) through (14). The derivations are provided in Appendix B. The variance σ^2 is a scalar whose value, $N_0/(2T_{CO})$, is not relevant to the development that follows and will be dropped for simplicity in notation. In

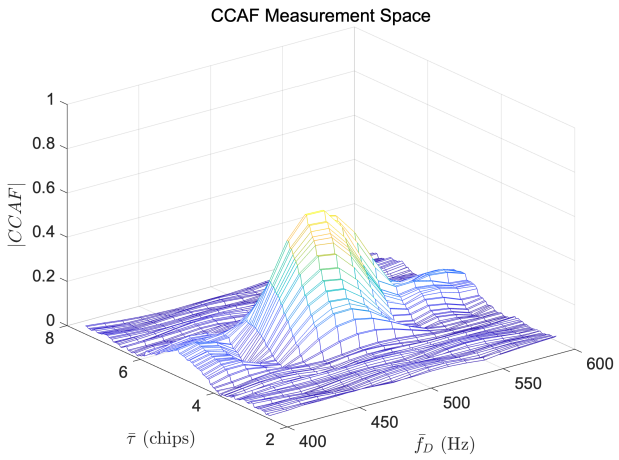

Fig. 12. Magnitude the spoofed GPS L1 C/A CCAF for C/N_0 = 45 dB-Hz and $T = 20$ ms when 2 signals are present in CCAF measurement space.

Signal	Parameter	x (true)	$\hat{x}$ (output)
Satellite	a_1	1	0.89
	τ_1	4.9	4.88
	f_{D_1}	495	494.53
	θ_1	0	6.18
Spoofed	a_2	0.9	0.74
	τ_2	5.1	5.12
	f_{D_2}	505	507.69
	θ_2	3.14	2.93
Multipath	a_3	0	0.05
	τ_3	0	6.23
	f_{D_3}	0	589.94
	θ_3	0	0

Table 4: A table showing the input and output parameters of the GPS L1 C/A CCAF for C/N_0 = 45 dB-Hz and $T = 20$ ms with the correlated measurement's cost function. The units are a (unitless), τ (chips), f_D (Hz), θ (rad).

this case

$$\mathrm{Cov}(z) = V_{2mn\times 2mn} = \mathrm{E}\begin{bmatrix} I_{11}I_{11} & I_{11}Q_{11} & I_{11}I_{21} & \cdots & I_{11}Q_{mn} \\ Q_{11}I_{11} & Q_{11}Q_{11} & Q_{11}I_{21} & \cdots & Q_{11}Q_{mn} \\ I_{21}I_{11} & I_{21}Q_{11} & I_{21}I_{21} & \cdots & I_{21}Q_{mn} \\ Q_{21}I_{11} & Q_{21}Q_{11} & Q_{21}I_{21} & \cdots & Q_{21}Q_{mn} \\ \vdots & \vdots & \vdots & \vdots & \vdots \\ Q_{mn}I_{11} & Q_{mn}I_{11} & Q_{mn}I_{21} & \cdots & Q_{mn}Q_{mn} \end{bmatrix}, \tag{11}$$

$$\mathrm{E}\left(I_{ij}I_{kl}\right) = \left(1 - \frac{|\bar{\tau}_j - \bar{\tau}_l|}{T_C}\right)\left\{\mathrm{sinc}\left(2\pi\left(\bar{f}_{D_i} - \bar{f}_{D_k}\right)T\right) + \mathrm{sinc}\left(2\pi\left(\bar{f}_{D_i} + \bar{f}_{D_k}\right)T\right)\right\}, \tag{12}$$

$$\mathrm{E}\left(Q_{ij}Q_{kl}\right) = \left(1 - \frac{|\bar{\tau}_j - \bar{\tau}_l|}{T_C}\right)\left\{\mathrm{sinc}\left(2\pi\left(\bar{f}_{D_i} - \bar{f}_{D_k}\right)T\right) - \mathrm{sinc}\left(2\pi\left(\bar{f}_{D_i} + \bar{f}_{D_k}\right)T\right)\right\}, \tag{13}$$

$$\mathrm{E}\left(I_{ij}Q_{kl}\right) = \mathrm{E}\left(Q_{ij}I_{kl}\right) = -\left(1 - \frac{|\bar{\tau}_j - \bar{\tau}_l|}{T_C}\right) \cdot \left\{\mathrm{sinc}\left(\pi\left(\bar{f}_{D_i} - \bar{f}_{D_k}\right)T\right)\sin\left(\pi\left(\bar{f}_{D_i} - \bar{f}_{D_k}\right)T\right) + \mathrm{sinc}\left(\pi\left(\bar{f}_{D_i} + \bar{f}_{D_k}\right)T\right)\sin\left(\pi\left(\bar{f}_{D_i} + \bar{f}_{D_k}\right)T\right)\right\}, \tag{14}$$

and i and k are the indices of the Doppler frequencies $\left(\bar{f}_D\right)$, which vary from 1 to m, and j and l are the indices of the code delays $(\bar{\tau})$, which vary from 1 to n.

We can write our measurement model in the general form

$$z = S_N\left(x \mid \bar{\tau}, \bar{f}_D\right) + v \tag{15}$$

where

$$v \sim N\left(0, V\right). \tag{16}$$

Weighting (i.e., 'whitening') our measurements, we obtain

$$z' = V^{-\frac{1}{2}}z = V^{-\frac{1}{2}}S_N\left(x \mid \bar{\tau}, \bar{f}_D\right) + v' \tag{17}$$

where

$$v' \sim N\left(0, I_{2mn\times 2mn}\right). \tag{18}$$

The final measurement model is then

$$z' = V^{-\frac{1}{2}}S_N\left(x \mid \bar{\tau}, \bar{f}_D\right) + v'. \tag{19}$$

To decompose the signal into its constituent elements, we then seek the parameter vector $\widehat{x}$ to minimize the cost function

$$J = \left\| z' - V^{-\frac{1}{2}}S_N\left(\widehat{x} \mid \bar{\tau}, \bar{f}_D\right)\right\|^2. \tag{20}$$

As C/N_0 is lowered, the measurement error variance increases exponentially. In these cases, it is expected that the accuracy of CCAF decomposition attained by minimizing Equation (20) using decorrelated measurements should be superior to that obtained by minimizing the unweighted cost function in Equation (9). This is investigated further in the next section.

VII. COVARIANCE ANALYSIS

To evaluate the potential performance gain using decorrelated measurements relative to the raw (correlated) original ones, we use the test scenario with three component signals (authentic, spoofed, and multipath) in Table 5. The scenario is the same as the one used in the previous examples. The code delay discrepancy between the authentic and spoofed signals is 0.2 chips, and the difference in Doppler frequency is 10 Hz. Additionally, there is a phase difference of π radians between the two signals. The multipath signal has a relatively lower amplitude compared to the authentic and spoofed signals.

We then linearize Equation (7) referenced to the true signal parameters to perform covariance analysis. The linearized covariance results will represent best case (lowest error variance) for estimation of the component signal parameters–i.e., the Cramer Rao Lower Bound (CRLB). We varied C/N_0 from 30 dB-Hz to 65 dB-Hz at intervals of 5 dB-Hz. We also perform 500 randomly seeded runs of the actual nonlinear PSO estimator at each C/N_0 to validate the covariance results.

In Figure 13, we show the estimate error of the authentic signal's amplitude, a_1, for both correlated and decorrelated measurements (depicted in blue), alongside the 1σ covariance envelope (highlighted in red). As expected the estimate error increases as C/N_0 is lowered.

Signal	Parameter	x (true)
Satellite	a_1	1.0
	τ_1	4.9
	f_{D1}	495
	θ_1	6.28
Spoofed	a_2	0.9
	τ_2	5.1
	f_{D2}	505
	θ_2	3.14
Multipath	a_3	0.3
	τ_3	4.8
	f_{D3}	490
	θ_3	1.57

Table 5: A table showing the true parameters of the GPS L1 C/A CCAF used for least squares error estimation. The units are a (unitless), τ (chips), f_D (Hz), θ (rad).

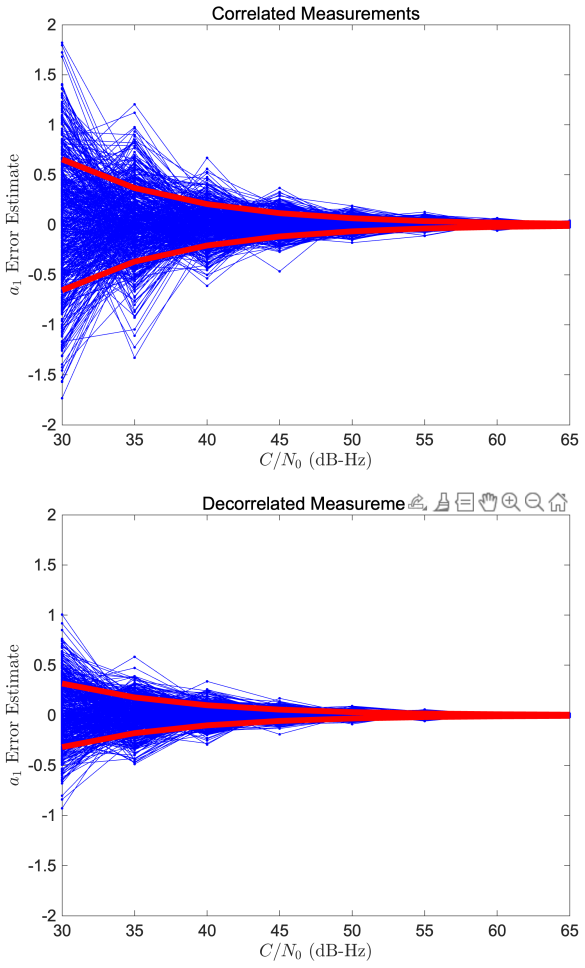

Fig. 13. Authentic amplitude a_1 error estimate runs for different C/N_0 (blue) and the 1σ envelope (red) for correlated (top) and decorrelated (bottom) measurements.

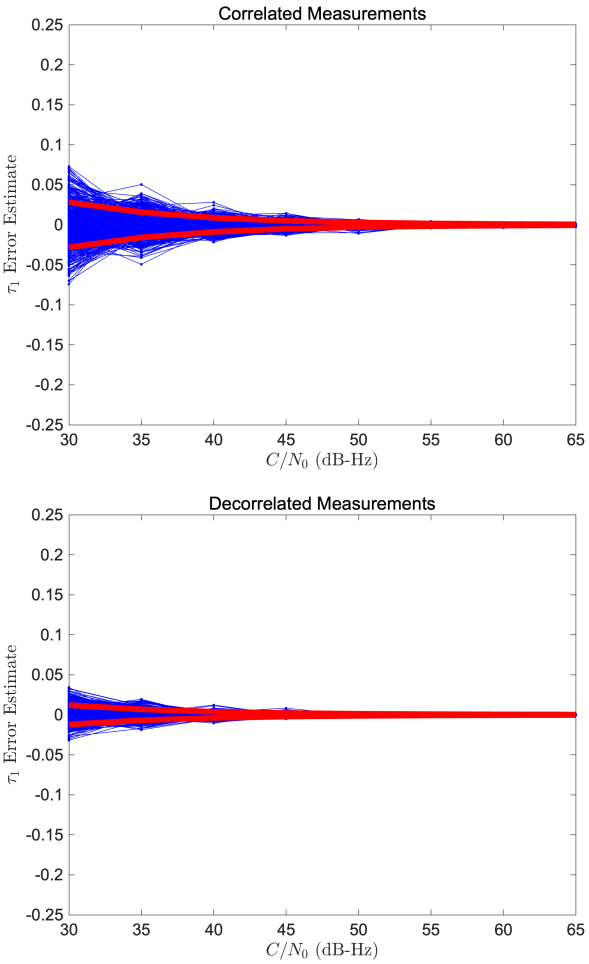

Fig. 14. Authentic code delay τ_1 (in chips) error estimate runs for different C/N_0 (blue) and the 1σ envelope (red) for correlated (top) and decorrelated (bottom) measurements.

The process of whitening the measurements leads to a reduction in the standard deviation at all values of C/N_0. At C/N_0 = 30 dB-Hz the error standard deviation (σ) is reduced from 0.65 to 0.31 for C/N_0 = 30 dB-Hz. For very high C/N_0, there is little difference in performance between the two methods.

Figure 14 shows the code delay estimate error for the authentic signal, τ_1. As anticipated, the decorrelated code delay τ_1 error is lower than the correlated code delay τ_1 error for all values of C/N_0. Figures 15 and 16 show similar results for the estimate errors in the authentic signal's Doppler f_{D1} and carrier phase θ_1.

For the decomposed spoofed and multipath signals, we show the code delay estimate errors, τ_2 and τ_3, for the correlated and decorrelated measurements in Figures 17 (τ_2) and 18 (τ_3). The estimate error for the multipath signal code delay, τ_3, is larger than for τ_2 and τ_1 (in Figure 14). This is attributable to the multipath signal's lower amplitude, set at 0.3, which makes it more difficult to detect through the additive noise.

Through the results of the covariance analysis and the associated randomized simulations, we verify that the estimate errors for all signal parameters are consistently

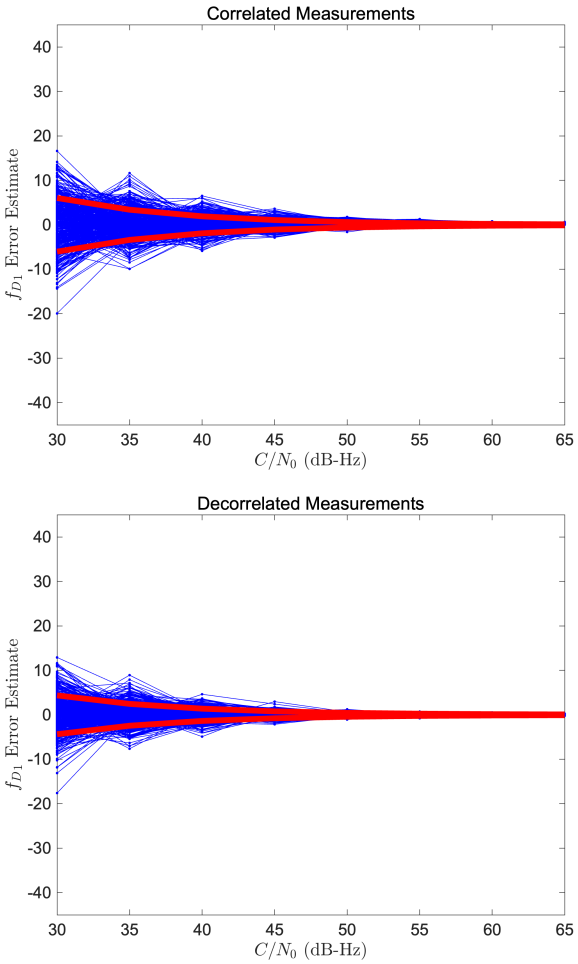

Fig. 15. Authentic Doppler frequency $f_{D\,1}$ (in Hz) error estimate runs for different C/N_0 (blue) and the 1σ envelope (red) for correlated (top) and decorrelated (bottom) measurements.

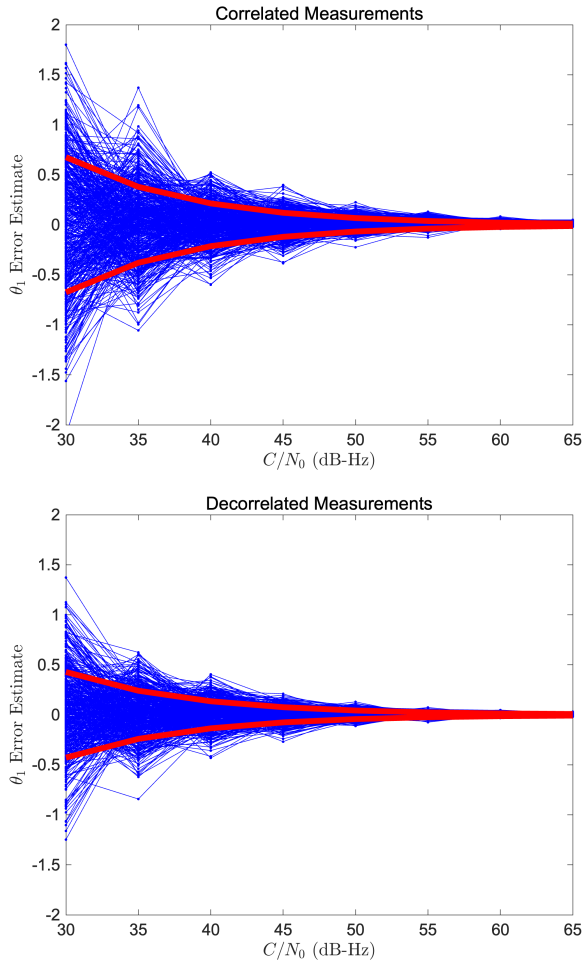

Fig. 16. Authentic carrier phase θ_1 (in radians) error estimate runs for different C/N_0 (blue) and the 1σ envelope (red) for correlated (top) and decorrelated (bottom) measurements.

lower using the decorrelated measurements compared to the correlated measurements. This conclusion holds across various other scenarios that we simulated. In the next section, we will delve deeper into the implications of these findings.

VIII. RESULTS AND DISCUSSION

In Table 4, we showed the output parameters of the CCAF with two signals present (no multipath) for C/N_0 = 45 dB-Hz obtained by decomposition using the correlated measurements and unweighted least-squares cost function in Equation (9). When we employ instead the weighted cost function in Equation (20) and the whitened measurements, we obtain the results in Table 6. In this case the output parameters are significantly closer to the true parameters for both the authentic and spoofed signals. Moreover, the amplitude of the multipath signal is estimated to be close to zero, correctly indicating that the CCAF measurement space is composed of only two signals.

The main objective of decorrelation is to mitigate the impact of thermal noise. To assess its effectiveness at even higher noise levels, we lower the C/N_0 to 35 dB-Hz and perform CCAF decomposition for the same scenario. Figure 19 illustrates the magnitude of the CCAF measurement space. The output parameters when using the correlated measurements for C/N_0 = 35 dB-Hz are in Table 7 and those obtained using the decorrelated measurements are in Table 8. It is evident that the parameter estimates for the authentic and spoofed signals are better using the decorrelated measurements, but both approaches yield a third low amplitude signal, likely due to a noise peak in the CCAF measurement space.

We now re-introduce multipath signals into the CCAF measurement space, as depicted in Figure 20. Table 9 presents the output parameters obtained using correlated measurements, while Table 10 displays the those acquired using the decorrelated measurements. Again, the parameter estimates for the authentic and spoofed signals are better using the decorrelated measurements, but in both cases the parameters for the multipath signal are noticeably off. This suggests that while decorrelation

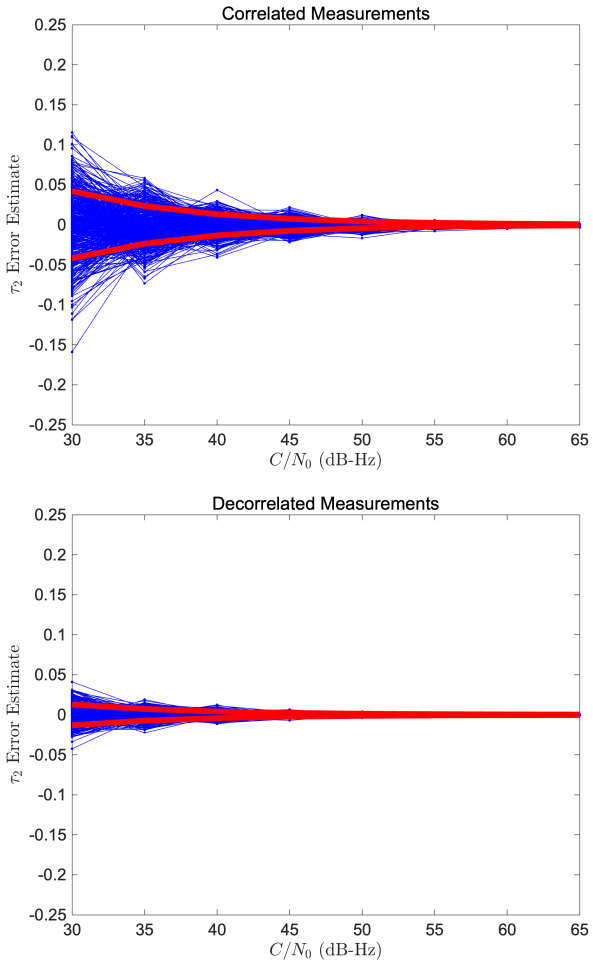

Fig. 17. Spoofed code delay τ_2 (in chips) error estimate runs for different C/N_0 (blue) and the 1σ envelope (red) for correlated (top) and decorrelated (bottom) measurements.

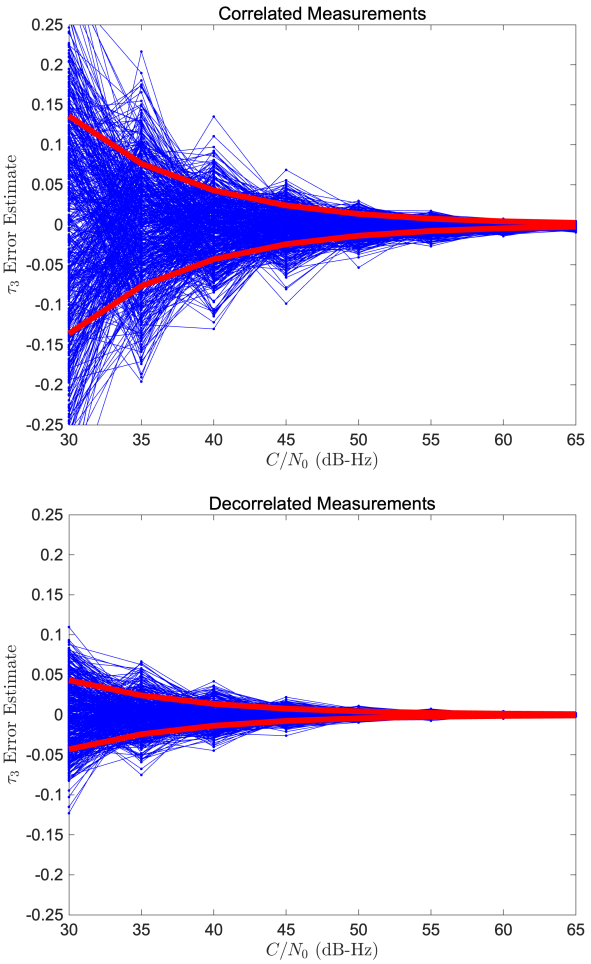

Fig. 18. Multipath code delay τ_3 (in chips) error estimate runs for different C/N_0 (blue) and the 1σ envelope (red) for correlated (top) and decorrelated (bottom) measurements.

improves the estimation accuracy for the authentic and spoofed signals, it might not be as effective in handling multipath signals because of their lower amplitude. From the point of view of spoofing detection, however, this is likely not a major concern.

Based on these results and those in the Section VII, it is clear that better performance is achieved through measurement decorrelation. One might legitimately comment this should have been expected at the outset because, after all, it is the proper way to deal with correlated measurements in a least squares estimator. Indeed, we also understood this at the outset. However, there is the parallel consideration of computational expense. The covariance matrix V can be very large, and its construction via Equations (12)–(14) and the operations required to execute the matrix square root and inversion in Equation (17) are not insignificant. For example, for the measurement space used in the examples so far the number of Doppler frequencies and code delays was $m = 17$ and $n = 250$, respectively, corresponding to a measurement covariance matrix of size $2mn \times 2mn = 8500 \times 8500$. This points to one reason why the uncorrelated approach was attempted first; the other being the non-trivial derivation of the covariance matrix itself (Appendix B).

However, there are several practical avenues to computational relief. First, the measurement space used in the examples is undoubtedly far larger than necessary to detect the subtle spoofing events that the CCAF decomposition method was developed to target. Cases where the code delays and Dopplers of the authentic and spoofed signals are very close to each other would hardly require observations over the range of ± 2.5 chips and ± 200 Hz. (Large offsets of the spoofing signal relative to the authentic are easily detectable by other, simpler monitors.) Second, the matrix $V^{-\frac{1}{2}}$ can be computed offline and stored. The structure of V is defined by the inputs to Equations (12)–(14), namely $\Delta\bar{\tau} \triangleq \bar{\tau}_l - \bar{\tau}_l$, $\Delta\bar{f}_D \triangleq \bar{f}_{D_i} - \bar{f}_{D_k}$, and $\bar{f}_D^+ \triangleq \bar{f}_{D_i} + \bar{f}_{D_k}$. The upper and lower limits on the first two can simply be set based on the limited range of offsets between the authentic and spoofed signals that the CCAF decomposition algorithm is intended to support. However, the third, $\bar{f}_D^+$, does require the additional knowledge of the current authentic Doppler. This is not difficult to come by, of course, but

as the stated desire is to have $V^{-\frac{1}{2}}$ pre-computed, this is a problem. Fortunately, it can be addressed in one of two ways: (1) compute and store multiple instantiations of $V^{-\frac{1}{2}}$ corresponding to different values of the true Doppler, such that the entire space of interest (e.g., $\pm$5000 Hz) is spanned by the $\bar{f}_D^+$ and $\Delta\bar{f}_D$ values used to produce the stored matrices, or (2) because the Doppler changes slowly over time, $V^{-\frac{1}{2}}$ can be computed online, but at a much slower update rate than the monitor's detection rate.

Signal	Parameter	x (true)	$\hat{x}$ (output)
Satellite	a_1	1	1.0
	τ_1	4.9	4.90
	f_{D1}	495	495.06
	θ_1	0	0
Spoofed	a_2	0.9	0.86
	τ_2	5.1	5.1
	f_{D2}	505	506.25
	θ_2	3.14	3.12
Multipath	a_3	0	0.06
	τ_3	0	5.12
	f_{D3}	0	479.70
	θ_3	0	4.33

Table 6: A table showing the input and output parameters of the GPS L1 C/A CCAF for C/N_0 = 45 dB-Hz and $T = 20$ ms with the decorrelated (whitened) measurements' cost function. The units are a (unitless), τ (chips), f_D (Hz), θ (rad).

Yet another option to mitigate the effects of thermal noise (without decorrelation) is to extend the coherent integration time T. Normally, the upper limit is imposed by duration of modulated navigation data bits, 20 ms for GPS L1 C/A signal. Ignoring this fact for the moment, we note that in addition to the obvious benefits in noise suppression, as we increase the coherent integration time, the sinc function in Figure 2 becomes narrower, with nulls at $1/T$. As a result, the Doppler frequency (f_D) resolution improves because the range of frequencies decreases. In reality, extended coherent integration times are also hindered by other factors in addition to unknown navigation data bits, most notably receiver oscillator phase noise and receiver motion. In this exercise, however, we are interested only in investigating the potential improvements in CCAF decomposition performance made possible by increased integration times. Hence, we assume the data bits are known, for example having been previously decoded with no intervening data changeovers, and with proper clock modelling and motion compensation. Some methods to do this are described in [18]. In the coming examples, we use a coherent integration time of $T = 100$ ms.

In Table 11, we present the output parameters of the three decomposed signals in comparison with the true parameters for at C/N_0 = 35 dB-Hz. Figure 21 shows the magnitude of the CCAF of the composite signal and noise. The output parameter estimates are obtained using correlated measurements and a coherent integration time T of 100 milliseconds. The results show that the CCAF

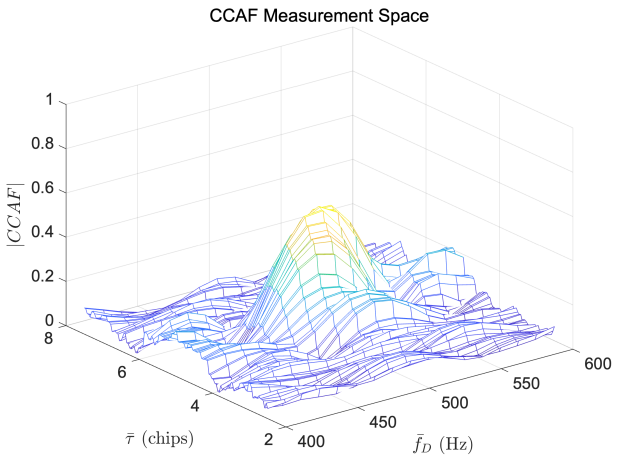

Fig. 19. Magnitude of the spoofed GPS L1 C/A CCAF for C/N_0 = 35 dB-Hz and $T = 20$ ms when 2 signals are present in the CCAF measurement space.

Signal	Parameter	x (true)	$\hat{x}$ (output)
Satellite	a_1	1	0.76
	τ_1	4.9	4.88
	f_{D1}	495	488.13
	θ_1	0	0.05
Spoofed	a_2	0.9	0.65
	τ_2	5.1	5.17
	f_{D2}	505	502.30
	θ_2	3.14	3.73
Multipath	a_3	0	0.43
	τ_3	0	5.31
	f_{D3}	0	473.88
	θ_3	0	2.79

Table 7: A table showing the input and output parameters of the GPS L1 C/A CCAF for C/N_0 = 35 dB-Hz and $T = 20$ ms with the correlated measurements' cost function. The units are a (unitless), τ (chips), f_D (Hz), θ (rad).

Signal	Parameter	x (true)	$\hat{x}$ (output)
Satellite	a_1	1	1.09
	τ_1	4.9	4.88
	f_{D1}	495	491.80
	θ_1	0	0.05
Spoofed	a_2	0.9	1.0
	τ_2	5.1	5.11
	f_{D2}	505	507.56
	θ_2	3.14	2.64
Multipath	a_3	0	0.33
	τ_3	0	5.48
	f_{D3}	0	521.36
	θ_3	0	4.02

Table 8: A table showing the input and output parameters of the GPS L1 C/A CCAF for C/N_0 = 35 dB-Hz and $T = 20$ ms with the decorrelated (whitened) measurements' cost function. The units are a (unitless), τ (chips), f_D (Hz), θ (rad).

decomposition yields better parameter estimates than those obtained with a 20-millisecond coherent integration time, even when the measurements are decorrelated. The improvement is due to the significant reduction in the

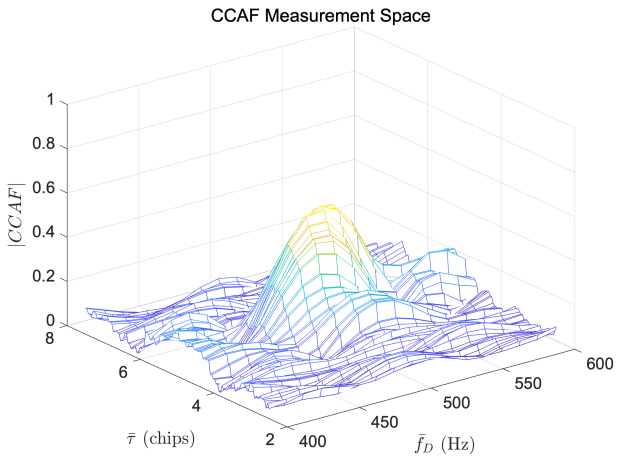

Fig. 20. Magnitude of the spoofed GPS L1 C/A CCAF for C/N_0 = 35 dB-Hz and $T = 20$ ms when 3 signals are present in the CCAF measurement space.

Signal	Parameter	x (true)	$\hat{x}$ (output)
Satellite	a_1	1	1.06
	τ_1	4.9	4.86
	f_{D1}	495	490.35
	θ_1	0	0.51
Spoofed	a_2	0.9	0.75
	τ_2	5.1	5.05
	f_{D2}	505	505.43
	θ_2	3.14	3.18
Multipath	a_3	0.3	0.19
	τ_3	4.8	4.60
	f_{D3}	490	400.00
	θ_3	1.57	5.82

Table 9: A table showing the input and output parameters of the GPS L1 C/A CCAF for C/N_0 = 35 dB-Hz and $T = 20$ ms with the correlated measurements' cost function. The units are a (unitless), τ (chips), f_D (Hz), θ (rad).

Signal	Parameter	x (true)	$\hat{x}$ (output)
Satellite	a_1	1	1.0
	τ_1	4.9	4.9
	f_{D1}	495	497.31
	θ_1	0	0.47
Spoofed	a_2	0.9	1.1
	τ_2	5.1	5.09
	f_{D2}	505	506.81
	θ_2	3.14	2.83
Multipath	a_3	0.3	0.58
	τ_3	4.8	4.89
	f_{D3}	490	498.79
	θ_3	1.57	5.54

Table 10: A table showing the input and output parameters of the GPS L1 C/A CCAF for C/N_0 = 35 dB-Hz and $T = 20$ ms with the decorrelated (whitened) measurements' cost function. The units are a (unitless), τ (chips), f_D (Hz), θ (rad).

noise floor with the longer integration period at lower carrier to noise density ratio.

Table 12 shows the results when only two signals are present (no multipath) but the algorithm is seeking three, again with C/N_0 = 35 dB-Hz. The magnitude of the CCAF is depicted in Figure 22. Once more, the output parameter estimates are obtained using correlated measurements and a coherent integration time T of 100 ms. Notably, the third signal has an estimated amplitude of zero, indicating the absence of a third signal in the CCAF measurement space.

These results suggest that the benefits of increasing the integration interval may be significant enough to warrant the extra effort needed to address the accompanying challenges, namely data bit prediction, motion compensation, and clock phase noise modeling. The first of these challenges could be mitigated by using GNSS pilot signals, such as L1C and L5 for GPS, but the remaining two would still need to be addressed [19].

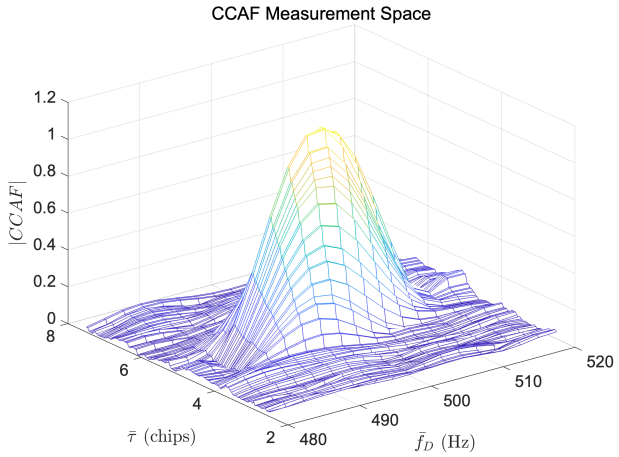

Fig. 21. Magnitude of the spoofed GPS L1 C/A CCAF for C/N_0 = 35 dB-Hz and $T = 100$ ms when 3 signals are present in the CCAF measurement space.

Signal	Parameter	x (true)	$\hat{x}$ (output)
Satellite	a_1	1	1.0
	τ_1	4.9	4.9
	f_{D1}	495	495.19
	θ_1	0	6.20
Spoofed	a_2	0.9	0.93
	τ_2	5.1	5.1
	f_{D2}	505	504.93
	θ_2	3.14	3.16
Multipath	a_3	0.3	0.37
	τ_3	4.8	4.86
	f_{D3}	490	489.77
	θ_3	1.57	1.76

Table 11: A table showing the input and output parameters of the the GPS L1 C/A CCAF for C/N_0 = 35 dB-Hz and $T = 100$ ms when 3 signals are present in CCAF measurement space with correlated measurements. The units are a (unitless), τ (chips), f_D (Hz), θ (rad).

IX. CONCLUSION

In this paper, we present a method for decomposing spoofed GNSS Complex Cross Ambiguity Functions

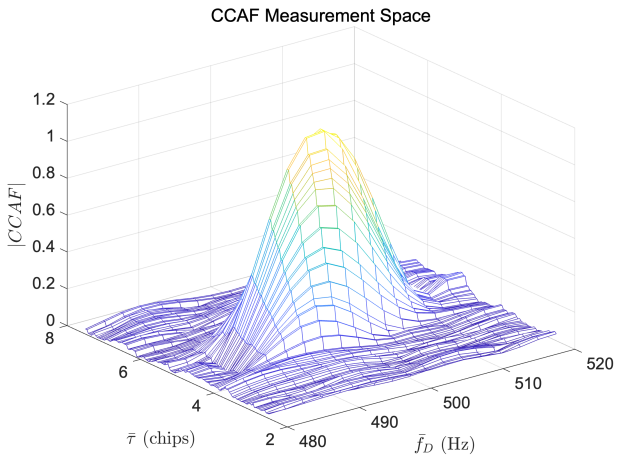

Fig. 22. Magnitude of the spoofed GPS L1 C/A CCAF for C/N_0 = 35 dB-Hz and $T = 100$ ms when 2 signals are present in the CCAF measurement space.

Signal	Parameter	x (true)	$\hat{x}$ (output)
Satellite	a_1	1	1.01
	τ_1	4.9	4.89
	f_{D1}	495	495.01
	θ_1	0	6.25
Spoofed	a_2	0.9	0.92
	τ_2	5.1	5.1
	f_{D2}	505	504.89
	θ_2	3.14	3.14
Multipath	a_3	0	0
	τ_3	0	5.4
	f_{D3}	0	502.12
	θ_3	0	4.39

Table 12: A table showing the input and output parameters of the GPS L1 C/A CCAF for C/N_0 = 35 dB-Hz and $T = 100$ ms when 2 signals are present in the CCAF measurement space with correlated measurements. The units are a (unitless), τ (chips), f_D (Hz), θ (rad).

(CCAF) into their constituent signals: authentic, spoofed, and multipath. We demonstrate the critical importance of using *complex* cross ambiguity measurements relative to the magnitude-only approaches utilized in prior work on spoofing detection. We show that the effects of code cross-correlation are relatively small, while thermal noise has a significant impact on signal decomposition performance. To address this challenge, we introduce a novel CCAF error decorrelation method aimed at mitigating the influence of thermal noise. Through numerical experimentation, we evaluate the performance of our decomposition algorithm across varying noise levels. Our results indicate that using decorrelated measurements leads to significantly lower estimate errors compared to correlated measurements, underscoring the efficacy of the new approach. Finally, we demonstrate the potential benefits in CCAF decomposition performance using extended coherent integration times to further reduce the effects of thermal noise.

APPENDIX A
PSO ALGORITHM

Let f be the function to be minimized. Generate n particles randomly with "positions" $p_i(t) \in \mathbb{P}$ and "velocities" $v_i(t) \in \mathbb{V}$. In our case, $p_i(t)$ is a 12×1 vector that represents amplitude a, code delay τ, Doppler frequency f_D and carrier phase θ for the authentic, spoofed and multipath signals. For each particle $i = 1, 2, \ldots, n$ positions p_i are updated using the following equation:

$$p_i(k+1) = p_i(k) + v_i(k+1) \tag{21}$$

and each particle moves in the parameter space with velocities v_i based on its own best positions l_i (i.e., the parameter vectors corresponding lowest J-value over the previous and current iterations) and the entire population's best position $g(k)$ as shown in Equation (22)

$$\begin{aligned} v_i(k+1) = w v_i(k) + c_1 r_1 \left[l_i(k) - p_i(k) \right] \\ + c_2 r_2 \left[g(k) - p_i(k) \right]. \end{aligned} \tag{22}$$

When a particle finds a position solution that leads to a lower cost function value than the previous ones, l_i gets updated:

$$l_i(k+1) = \begin{cases} l_i(k) & f\left(l_i(k)\right) \leq f\left(p_i(k+1)\right) \\ p_i(k+1) & f\left(l_i(k)\right) > f\left(p_i(k+1)\right) \end{cases}. \tag{23}$$

If that particle's position is the best among all other particles' positions (i.e., it minimizes the cost function across all current particles), g is updated based on Equation (24) and becomes the best global solution of the swarm

$$g(k+1) = \min\left\{ f\left(l_i(k)\right), f(g(k)) \right\}. \tag{24}$$

The following definitions apply to the equations above.

- r_1, r_2 are 12×1 vectors of uniformly distributed numbers with $U(0,1)$ selected independently at each iteration,
- w is the 'inertia' coefficient, and
- c_1, c_2 are the 'acceleration' coefficients.

The inertia coefficient (w) balances exploration and exploitation. A larger inertia weight facilitates global exploration, while a smaller inertia weight tends to facilitate local exploitation. We want to exploit the CCAF measurement space within ± 0.5 chips of code delay and ± 10 Hz of Doppler frequency around the best guess of the authentic signal, so we choose a smaller inertia coefficient. The so-called 'cognitive acceleration coefficient' (c_1) reflects the particle's tendency to return to its own best position. The 'social acceleration coefficient' (c_2) reflects the particle's tendency to move towards the swarm's best position. In our case, we tuned our parameters such that the social acceleration coefficient (c_2) is larger than the cognitive acceleration coefficient (c_1) since particles will be more strongly attracted to the global best position (g) found by the entire swarm and search in the vicinity of the global best position. The swarm is likely to converge more quickly to a solution

because particles will be more focused on moving towards the global best position. In this work, we selected w, c_1, c_2 as 0.5, 1 and 2, respectively.

APPENDIX B

DERIVATION OF THE CCAF COVARIANCE MATRIX

Definitions:

- $n(t)$ is a zero-mean white noise process with power spectral density of $N_0/2$
- $c(t)$ is a (pseudo)random code (± 1) with chip duration T_C
- τ is the code phase delay
- $\omega \triangleq 2\pi f$ is the carrier frequency, and
- $T \triangleq NT_C$ is the coherent averaging time defined by positive integer N.

The effect of the correlation and averaging operation on the noise is

$$\begin{aligned} n(T,\tau,\omega) &= \frac{1}{T}\int_0^T c(t-\tau)n(t)e^{-j\omega t}dt \\ &= n_I(T,\tau,\omega) + jn_Q(T,\tau,\omega). \end{aligned} \tag{25}$$

The means of $n_I(T,\tau,\omega)$ and $n_Q(T,\tau,\omega)$ are clearly both zero because $n(t)$ is zero-mean. However, the covariances are not so easily determined. We first consider the case $E\{n_I(T,\tau_1,\omega_1)\, n_I(T,\tau_2,\omega_2)\}$ with $\tau_2 \geq \tau_1$, $\tau_2 - \tau_1 \leq T_C$.

$$\begin{aligned} &E\{n_I(T,\tau_1,\omega_1)\, n_I(T,\tau_2,\omega_2)\} \\ &= E\left\{\left(\frac{1}{T}\sum_{n=0}^{N-1}\int_{nT_C+\tau_2}^{(n+1)T_C+\tau_1} n(t_1)\cos(\omega_1 t_1)\,dt_1\right)\right. \\ &\quad \left.\cdot\left(\frac{1}{T}\sum_{n=0}^{N-1}\int_{nT_C+\tau_2}^{(n+1)T_C+\tau_1} n(t_2)\cos(\omega_2 t_2)\,dt_2\right)\right\} \end{aligned} \tag{26}$$

$$\begin{aligned} &= \frac{1}{T^2}\sum_{n=0}^{N-1}\int_{nT_C+\tau_2}^{(n+1)T_C+\tau_1}\cos(\omega_1 t_1)\cdot \\ &\quad \sum_{n=0}^{N-1}\int_{nT_C+\tau_2}^{(n+1)T_C+\tau_1} E\{n(t_1)\,n(t_2)\}\cos(\omega_2 t_2)\,dt_2 dt_1 \end{aligned} \tag{27}$$

$$\begin{aligned} &= \frac{1}{T^2}\sum_{n=0}^{N-1}\int_{nT_C+\tau_2}^{(n+1)T_C+\tau_1}\cos(\omega_1 t_1)\cdot \\ &\quad \sum_{n=0}^{N-1}\int_{nT_C+\tau_2}^{(n+1)T_C+\tau_1} \frac{N_0}{2}\delta(t_1-t_2)\cos(\omega_2 t_2)\,dt_2 dt_1 \end{aligned} \tag{28}$$

$$= \frac{N_0}{2T^2}\sum_{n=0}^{N-1}\int_{nT_C+\tau_2}^{(n+1)T_C+\tau_1}\cos(\omega_1 t_1)\cos(\omega_2 t_1)\,dt_1 \tag{29}$$

$$\begin{aligned} &= \frac{N_0}{4T^2}\sum_{n=0}^{N-1}\left\{\left.\frac{\sin((\omega_1-\omega_2)t)}{\omega_1-\omega_2}\right|_{nT_C+\tau_2}^{(n+1)T_C+\tau_1}\right. \\ &\quad \left.+\left.\frac{\sin((\omega_1+\omega_2)t)}{\omega_1+\omega_2}\right|_{nT_C+\tau_2}^{(n+1)T_C+\tau_1}\right\} \end{aligned} \tag{30}$$

$$\begin{aligned} &E\{n_I(T,\tau_1,\omega_1,)\, n_I(T,\tau_2,\omega_2,)\} \\ &= \frac{N_0}{4T^2}\sum_{n=0}^{N-1}\left\{\left[\frac{\sin((\omega_1-\omega_2)((n+1)T_C+\tau_1))}{\omega_1-\omega_2}\right.\right. \\ &\quad \left.-\frac{\sin((\omega_1-\omega_2)(nT_C+\tau_2))}{\omega_1-\omega_2}\right] \\ &\quad +\left[\frac{\sin((\omega_1+\omega_2)((n+1)T_C+\tau_1))}{\omega_1+\omega_2}\right. \\ &\quad \left.\left.-\frac{\sin((\omega_1+\omega_2)(nT_C+\tau_2))}{\omega_1+\omega_2}\right]\right\} \end{aligned} \tag{31}$$

We now simplify notation on the left side by defining

$$E\left\{n_I(T)^2_{1,2}\right\} \triangleq E\{n_I(T,\tau_1,\omega_1,)\, n_I(T,\tau_2,\omega_2,)\}, \tag{32}$$

and break the right side into multiple parts,

$$E\left\{n_I(T)^2_{1,2}\right\} = \frac{N_0}{2T^2}\sum_{n=0}^{N-1}\left[\frac{A-B}{\omega_1-\omega_2}+\frac{C-D}{\omega_1+\omega_2}\right], \tag{33}$$

which allows us to use the following known result for the summation of a finite trigonometric series:

$$\sum_{n=0}^{N-1}\sin(a_1+bn) = \frac{\sin(Nb/2)}{\sin(b/2)}\sin(a_1+(N-1)b/2). \tag{34}$$

For term A we have

$$\begin{aligned} a_1 &= (\omega_1-\omega_2)(T_C+\tau_1) \\ b &= (\omega_1-\omega_2)T_C \end{aligned}$$

so that

$$\begin{aligned} A &= \sum_{n=0}^{N-1}\sin(a_1+bn) \\ &= \frac{\sin((\omega_1-\omega_2)T/2)}{\sin((\omega_1-\omega_2)T_C/2)}\cdot \\ &\quad \sin((\omega_1-\omega_2)(T_C+\tau_1)+(\omega_1-\omega_2)(N-1)T_C/2) \\ &= \frac{\sin((\omega_1-\omega_2)T/2)}{\sin((\omega_1-\omega_2)T_C/2)}\sin((\omega_1-\omega_2)(T/2+T_C/2+\tau_1)). \end{aligned}$$

For B,

$$\begin{aligned} a_2 &= (\omega_1-\omega_2)\tau_2 \\ b &= (\omega_1-\omega_2)T_C \end{aligned}$$

$$\begin{aligned} B &= \sum_{n=0}^{N-1}\sin(a_2+bn) \\ &= \frac{\sin((\omega_1-\omega_2)T/2)}{\sin((\omega_1-\omega_2)T_C/2)}\cdot \\ &\quad \cdot\sin((\omega_1-\omega_2)\tau_2+(\omega_1-\omega_2)(N-1)T_C/2) \\ &= \frac{\sin((\omega_1-\omega_2)T/2)}{\sin((\omega_1-\omega_2)T_C/2)} \\ &\quad \cdot\sin((\omega_1-\omega_2)(T/2-T_C/2+\tau_1)) \end{aligned}$$

Similarly, for C and D, we need only replace $(\omega_1 - \omega_2)$ with $(\omega_1 + \omega_2)$ in the results for A and B, respectively:

$$C = \sum_{n=0}^{N-1} \sin\left(c_1 + dn\right) = \frac{\sin\left(\left(\omega_1 + \omega_2\right) T/2\right)}{\sin\left(\left(\omega_1 + \omega_2\right) T_C/2\right)} \cdot \sin\left(\left(\omega_1 + \omega_2\right)\left(T/2 + T_C/2 + \tau_1\right)\right),$$

$$D = \sum_{n=0}^{N-1} \sin\left(c_2 + dn\right) = \frac{\sin\left(\left(\omega_1 + \omega_2\right) T/2\right)}{\sin\left(\left(\omega_1 + \omega_2\right) T_C/2\right)} \cdot \sin\left(\left(\omega_1 + \omega_2\right)\left(T/2 + T_C/2 + \tau_1\right)\right).$$

Bringing all the parts back together, we obtain

$$\begin{aligned} E\left\{n_I(T)_{1,2}^2\right\} = \frac{N_0}{4T^2}\Bigg\{ & \frac{1}{\omega_1 - \omega_2}\frac{\sin\left((\omega_1 - \omega_2)T/2\right)}{\sin\left((\omega_1 - \omega_2)T_C/2\right)} \\ & \cdot \left[\sin\left(\left(\omega_1 - \omega_2\right)\left(T/2 + T_C/2 + \tau_1\right)\right)\right. \\ & \left. - \sin\left(\left(\omega_1 - \omega_2\right)\left(T/2 - T_C/2 + \tau_2\right)\right)\right] \\ & + \frac{1}{\omega_1 + \omega_2}\frac{\sin\left((\omega_1 + \omega_2)T/2\right)}{\sin\left((\omega_1 + \omega_2)T_C/2\right)} \\ & \cdot \left[\sin\left(\left(\omega_1 + \omega_2\right)\left(T/2 + T_C/2 + \tau_1\right)\right)\right. \\ & \left. - \sin\left(\left(\omega_1 + \omega_2\right)\left(T/2 - T_C/2 + \tau_2\right)\right)\right]\Bigg\}. \end{aligned} \tag{35}$$

Knowing that $T \gg T_C, |\tau_1|$, and $|\tau_2|$, and for $\delta X/\bar{X} \ll 1$,

$$\sin(\alpha X + \beta) \approx \sin(\alpha \bar{X} + \beta) + \alpha \cos(\alpha \bar{X} + \beta)\delta X,$$

we can express the last result as

$$\begin{aligned} & E\left\{n_I(T)_{1,2}^2\right\} \\ & = \frac{N_0}{8T}\Bigg\{\frac{\operatorname{sinc}\left((\omega_1 - \omega_2)T/2\right)}{\sin\left((\omega_1 - \omega_2)T_C/2\right)} \\ & \cdot \left[(\omega_1 - \omega_2)\cos\left((\omega_1 - \omega_2)T/2\right)\left(T_C + \tau_1 - \tau_2\right)\right] \\ & \quad + \frac{\operatorname{sinc}\left((\omega_1 + \omega_2)T/2\right)}{\sin\left((\omega_1 + \omega_2)T_C/2\right)} \\ & \cdot \left[(\omega_1 + \omega_2)\cos\left((\omega_1 + \omega_2)T/2\right)\left(T_C + \tau_1 - \tau_2\right)\right]\Bigg\} \end{aligned} \tag{36}$$

$$\begin{aligned} & E\left\{n_I(T)_{1,2}^2\right\} \\ & \quad = \frac{N_0}{4T}\Bigg\{\frac{\operatorname{sinc}\left((\omega_1 - \omega_2)T/2\right)}{\operatorname{sinc}\left((\omega_1 - \omega_2)T_C/2\right)} \\ & \quad \cdot \left[\cos\left((\omega_1 - \omega_2)T/2\right)\left(1 - \frac{\tau_2 - \tau_1}{T_C}\right)\right] \\ & \quad\quad + \frac{\operatorname{sinc}\left((\omega_1 + \omega_2)T/2\right)}{\operatorname{sinc}\left((\omega_1 + \omega_2)T_C/2\right)} \\ & \quad \cdot \left[\cos\left((\omega_1 + \omega_2)T/2\right)\left(1 - \frac{\tau_2 - \tau_1}{T_C}\right)\right]\Bigg\} \end{aligned} \tag{37}$$

Knowing that $|\omega_1 \pm \omega_2|\, T_C/2 \ll 1$, we also know that $\operatorname{sinc}\left(\left(\omega_1 \pm \omega_2\right) T_C/2\right) \approx 1$, and therefore

$$\begin{aligned} & E\left\{n_I(T)_{1,2}^2\right\} = \frac{N_0}{2T}\left(1 - \frac{\tau_2 - \tau_1}{T_C}\right) \\ & \cdot \left\{\operatorname{sinc}\left(\left(\omega_1 - \omega_2\right) T/2\right)\cos\left(\left(\omega_1 - \omega_2\right) T/2\right)\right. \\ & \left. + \operatorname{sinc}\left(\left(\omega_1 - \omega_2\right) T/2\right)\cos\left(\left(\omega_1 + \omega_2\right) T/2\right)\right\} \end{aligned} \tag{38}$$

Now using the following identities,

$$\operatorname{sinc} x \cos x = \frac{\sin x}{x}\cos x = \frac{\sin 2x}{2x} = \operatorname{sinc} 2x$$

we can write

$$\begin{aligned} E\left\{n_I(T)_{1,2}^2\right\} = & \frac{N_0}{2T}\left(1 - \frac{\tau_2 - \tau_1}{T_C}\right) \\ & \left\{\operatorname{sinc}\left(\left(\omega_1 - \omega_2\right) T\right) + \operatorname{sinc}\left(\left(\omega_1 + \omega_2\right) T\right)\right\}. \end{aligned} \tag{39}$$

Recall that at the outset, we assumed that $\tau_2 \geq \tau_1$, so in the opposite case we may simply interchange the two. The general result may then be expressed simply as

$$\begin{aligned} E\left\{n_I\left(T, \tau_1, \omega_1\right) n_I\left(T, \tau_2, \omega_2\right)\right\} = & \frac{N_0}{2T}\left(1 - \frac{|\tau_2 - \tau_1|}{T_C}\right) \\ & \cdot \left\{\operatorname{sinc}\left(\left(\omega_1 - \omega_2\right) T\right) + \operatorname{sinc}\left(\left(\omega_1 + \omega_2\right) T\right)\right\}. \end{aligned} \tag{40}$$

Following the same process, we can show that

$$\begin{aligned} E\left\{n_Q\left(T, \tau_1, \omega_1\right) n_Q\left(T, \tau_2, \omega_2\right)\right\} = & \frac{N_0}{2T}\left(1 - \frac{|\tau_2 - \tau_1|}{T_C}\right) \\ & \cdot \left\{\operatorname{sinc}\left(\left(\omega_1 - \omega_2\right) T\right) - \operatorname{sinc}\left(\left(\omega_1 + \omega_2\right) T\right)\right\}, \end{aligned} \tag{41}$$

and

$$\begin{aligned} & E\left\{n_I\left(T, \tau_1, \omega_1\right) n_Q\left(T, \tau_2, \omega_2\right)\right\} \\ & = E\left\{n_Q\left(T, \tau_1, \omega_1\right) n_I\left(T, \tau_2, \omega_2\right)\right\} \\ & = -\frac{N_0}{2T}\left(1 - \frac{|\tau_2 - \tau_1|}{T_C}\right) \\ & \quad \cdot \left\{\operatorname{sinc}\left(\left(\omega_1 - \omega_2\right) T/2\right)\sin\left(\left(\omega_1 - \omega_2\right) T/2\right)\right. \\ & \quad \left. + \operatorname{sinc}\left(\left(\omega_1 + \omega_2\right) T/2\right)\sin\left(\left(\omega_1 + \omega_2\right) T/2\right)\right\} \end{aligned} \tag{42}$$

ACKNOWLEDGEMENT

We would like to thank our sponsors at the Federal Aviation Administration (FAA) and the Center for Assured and Resilient Navigation in Advanced TransportatION Systems (CARNATIONS) under the US Department of Transportation (USDOT)'s University Transportation Center (UTC) program for supporting this research. The views and opinions expressed in this paper are those of the authors and do not necessarily reflect those of any other organization or person.

REFERENCES

[1] I. Fernández-Hernández, T. Walter, K. Alexander, B. Clark, E. Châtre, C. Hegarty, M. Appel and M. Meurer, "Increasing International Civil Aviation Resilience: A Proposal for Nomenclature, Categorization and Treatment of New Interference Threats," in Proceedings of the 2019 International Technical Meeting of The Institute of Navigation, Reston, Virginia, January 2019.

[2] M. L. Psiaki and T. E. Humphreys, "GNSS Spoofing and Detection," Proceedings of the IEEE, vol. 104, no. 6, pp. 1258-1270, June 2016.

[3] D. M. Akos, "Who's Afraid of the Spoofer? GPS/GNSS Spoofing Detection via Automatic Gain Control (AGC).," Journal of the Institute of Navigation , vol. 59, no. 4, pp. 281-290, 2012.

[4] M. Pini, M. Fantino, A. Cavaleri, S. Ugazio and L. L. Presti, "Signal Quality Monitoring Applied to Spoofing Detection," in Proceedings of the 24th International Technical Meeting of the Satellite Division of The Institute of Navigation (ION GNSS 2011), Portland OR, 2011.

[5] S. Khanafseh, N. Roshan, S. Langel, F.-C. Chan, M. Joerger and B. Pervan, "GPS spoofing detection using RAIM with INS coupling," in 2014 IEEE/ION Position, Location and Navigation Symposium - PLANS 2014, Monterey, CA, USA, 2014.
[6] M. L. Psiaki, S. P. Powell and B. W. O'Hanlon, "GNSS Spoofing Detection using High-Frequency Antenna Motion and Carrier-Phase Data," in Proceedings of the 26th International Technical Meeting of the Satellite Division of The Institute of Navigation (ION GNSS+ 2013), Nashville, TN, September 16 - 20, 2013.
[7] C. Tanil, "Detecting GNSS Spoofing Attacks Using INS Coupling," in Ph.D. Dissertation, Department of Mechanical and Aerospace Engineering, Illinois Institute of Technology, Chicago, IL, 2016.
[8] L. Scott , "Anti-Spoofing and Authenticated Signal Architectures for Civil Navigation Systems," in Proceedings of the 16th International Technical Meeting of the Satellite Division of The Institute of Navigation (ION GPS/GNSS 2003), Portland, OR, September, 2003.
[9] P. Borhani-Darian, H. Li, P. Wu and P. Closas, "Deep Neural Network Approach to Detect GNSS Spoofing Attacks," in Proceedings of the 33rd International Technical Meeting of the Satellite Division of The Institute of Navigation (ION GNSS+ 2020).
[10] E. G. Manfredini, D. M. Akos, Y.-H. Chen, S. Lo, T. Walter and P. Enge, "Effective GPS Spoofing Detection Utilizing Metrics from Commercial Receivers," in Proceedings of the 2018 International Technical Meeting of The Institute of Navigation, Reston, Virginia, 2018.
[11] C. Hegarty, B. O'Hanlon, A. Odeh, K. Shallberg and J. Flake, "Spoofing Detection in GNSS Receivers through Cross Ambiguity Function Monitoring," in Proceedings of the 32nd International Technical Meeting of the Satellite Division of The Institute of Navigation (ION GNSS+ 2019), Miami, Florida, 2019.
[12] S. Ahmed, S. Khanafseh and B. Pervan, "GNSS Spoofing Detection based on Decomposition of the Complex Cross Ambiguity Function," in Proceedings of the 34th International Technical Meeting of the Satellite Division of The Institute of Navigation (ION GNSS+ 2021), St. Louis, Missouri, 2021.
[13] S. Ahmed, S. Khanafseh and B. Pervan, "Complex Cross Ambiguity Function Post-Decomposition Spoofing Detection with Inverse RAIM," in Proceedings of the 35th International Technical Meeting of the Satellite Division of The Institute of Navigation (ION GNSS+ 2022), Denver, Colorado, 2022.
[14] S. Ahmed, S. Khanafseh and B. Pervan, "Spoofing Detection using Decomposition of the Complex Cross Ambiguity Function with Measurement Correlation," 2023 IEEE/ION Position, Location and Navigation Symposium (PLANS), Monterey, CA, USA, 2023, pp. 500-510.
[15] R. D. J. van Nee, "The Multipath Estimating Delay Lock Loop," in IEEE Second International Symposium on Spread Spectrum Techniques and Applications, Yokohama, Japan, 1992.
[16] S. Ahmed, S. Khanafseh and B. Pervan, "GNSS Spoofing Detection and Exclusion by Decomposition of Complex Cross Ambiguity Function (DCCAF) with INS Aiding," in Proceedings of the 36th International Technical Meeting of the Satellite Division of The Institute of Navigation (ION GNSS+ 2023), Denver, Colorado, September 2023.
[17] K. Borre, D. Akos, N. Bertelsen, P. Rinder and S. H. Jensen, A Software-Defined GPS and Galileo Receiver:A Single-Frequency Approach, Boston, MA: Birkhäuser .
[18] J. Kennedy and R. Eberhart, "Particle swarm optimization," in Proceedings of ICNN'95 - International Conference on Neural Networks, 1995, pp. 1942-1948 vol.4, doi: 10.1109/ICNN.1995.488968.
[19] S. Ahmed, S. Khanafseh and B. Pervan, "Detecting GNSS Spoofing by Decomposition of the Complex Cross Ambiguity Function with Extended Coherent Integration Time," in ION 2024 Pacific PNT Meeting, Honolulu, HI, 2024.

Sahil Ahmed is currently a Ph.D. Candidate at the Navigation Laboratory in the Department of Mechanical and Aerospace Engineering, Illinois Institute of Technology (IIT). He also works as Navigation Engineer at Trunav. His research interests include Spoofing Detection in GNSS receivers, Software-Defined Radios (SDR), Satellite Communication, Statistical Signal Processing, Estimation and Tracking, Sensor Fusion for autonomous systems.

Dr. Samer Khanafseh (Member, IEEE), is currently a research associate professor at Illinois Institute of Technology (IIT), Chicago. He received his PhD degrees in Aerospace Engineering from IIT in 2008. Dr. Khanafseh has been involved in several aviation applications such as Autonomous Airborne Refueling (AAR) of unmanned air vehicles, autonomous shipboard landing for the NUCAS and JPALS programs, and the Ground Based Augmentation System (GBAS). His research interests are focused on high accuracy and high integrity navigation algorithms, cycle ambiguity resolution, high integrity applications, fault monitoring, and robust estimation techniques. He is an associate editor of IEEE Transactions on Aerospace and Electronic Systems and was the recipient of the 2011 Institute of Navigation Early Achievement Award for his outstanding contributions to the integrity of carrier phase navigation systems.

Dr. Boris Pervan (Senior Member, IEEE), is a Professor of Mechanical and Aerospace Engineering at IIT, where he conducts research on advanced navigation systems. Prior to joining the faculty at IIT, he was a spacecraft mission analyst at Hughes Aircraft Company (now Boeing) and a postdoctoral research associate at Stanford University. Prof. Pervan received his B.S. from the University of Notre Dame, M.S. from the California Institute of Technology, and Ph.D. from Stanford University. He has received the Samuel M. Burka and Johannes Kepler Awards from the Institute of Navigation (ION), IIT Sigma Xi Excellence in University Research Award (twice), IIT University Excellence in Teaching Award, IEEE Aerospace and Electronic Systems Society M. Barry Carlton Award, RTCA William E. Jackson Award, Guggenheim Fellowship (Caltech), and the Albert J. Zahm Prize in Aeronautics (Notre Dame). He is a Fellow of the ION, and former Editor-in-Chief of its peer-reviewed journal, NAVIGATION.